Particle-in-cell simulations of nonlocal and nonlinear effects in inductively coupled plasmas

A Thesis Submitted to the
College of Graduate Studies and Research
in Partial Fulfillment of the Requirements
for the degree of Master of Science
in the Department of Physics and Engineering Physics
University of Saskatchewan
Saskatoon

By
Aaron Froese

Permission to Use

In presenting this thesis in partial fulfilment of the requirements for a Postgraduate degree from the University of Saskatchewan, I agree that the Libraries of this University may make it freely available for inspection. I further agree that permission for copying of this thesis in any manner, in whole or in part, for scholarly purposes may be granted by the professor or professors who supervised my thesis work or, in their absence, by the Head of the Department or the Dean of the College in which my thesis work was done. It is understood that any copying or publication or use of this thesis or parts thereof for financial gain shall not be allowed without my written permission. It is also understood that due recognition shall be given to me and to the University of Saskatchewan in any scholarly use which may be made of any material in my thesis.

Requests for permission to copy or to make other use of material in this thesis in whole or part should be addressed to:

Head of the Department of Physics and Engineering Physics
163 Physics Building
116 Science Place
University of Saskatchewan
Saskatoon, Saskatchewan
Canada
S7N 5E2

Abstract

The kinetic effects in an inductively coupled plasma (ICP) due to thermal motion of particles modified by self-consistent magnetic fields are studied by using a particle-in-cell (PIC) simulation. In the low pressure, low frequency regime, electron mean free paths are large relative to device size and the trajectories are strongly curved by the induced radio frequency (RF) magnetic field. This causes problems for linear theories, which ignore the influence of the magnetic field on the particles, and are therefore unable to recover effects accumulated along each nonlinear path.

The tools to perform high-performance parallel PIC simulations of inductively coupled plasmas were developed to allow rapid scanning of a broad range of the input parameters, such as wave amplitude, frequency, and plasma temperature. Different behavioural regimes are identified by observing the resultant variations in the skin depth, surface impedance, and ponderomotive force (PMF). At low electron-neutral collision rates, these are shown to include the local collisionless regime, the anomalous skin effect regime, and the nonlinear regime.

The local collisionless regime occurs at high driving frequencies and is characterized by plasma behaviour independent of both the driving frequency and amplitude: a short skin depth, low energy absorption, and strong PMF. The anomalous skin effect regime occurs at low frequencies and low amplitudes: the plasma varies with driving frequency, but not driving amplitude, the skin depth increases with frequency, the plasma is much more absorptive in the anomalous regime than in the local regime, and the PMF increases with frequency. The nonlinear regime occurs at low frequencies and high amplitudes: the plasma varies with driving amplitude, but not frequency, the skin depth decreases with amplitude, there is low energy absorption, and the PMF increases with wave amplitude.

The simulation runs in four modes: linear collisionless, linear collisional, nonlinear collisionless, and nonlinear collisional. The linear modes, in which the particles ignore the magnetic field, are used to validate the results against theory, while the nonlinear modes are used to test actual plasma behaviour. In linear collisionless mode, the plasma was found to exhibit only the local collisionless and anomalous skin effect regimes, as expected by theories. In nonlinear collisionless mode, the plasma exhibits the nonlinear regime in addition to the regimes found in linear mode. Finally, the nonlinear regime disappears in nonlinear collisionless mode because the curved paths

caused by the magnetic field are disrupted by collisions.

Finally, the regime boundaries are investigated as a function of temperature. Since the plasma properties vary continuously, a boundary exists where two regimes share the same characteristics. From linear theories, it is known that the division between the local collisionless and anomalous skin effect regimes moves to higher frequencies as the plasma temperature is increased. When nonlinear fields are present, this still occurs, but in conjunction with the boundary between the local collisionless and nonlinear regimes moving to higher wave amplitudes. Temperature also effects the boundary between the anomalous skin effect and nonlinear regimes, causing the minimum frequency of the anomalous skin effect regime to be reduced at low wave amplitudes.

Acknowledgements

I am indebted to Andrei Smolyakov for his invaluable assistance and direction and to Dima Sydorenko for the use of and help understanding his programs. Research funding was provided by the University of Saskatchewan and NSERC. All computing was performed on Westgrid facilities.

Contents

List of Tables

List of Figures

List of Abbreviations

AC	alternating current
CIC	cloud-in-cell
CPU	central processing unit
DC	direct current
EM	electromagnetic
ICP	inductively coupled plasma
MPI	Message Passing Interface - a parallelization library
NGP	nearest grid point
NL	nonlinear
PIC	particle-in-cell
PMF	ponderomotive force
RF	radio frequency

List of Symbols

$a = \nu/\omega$	collisionality parameter
B_0	magnetic field amplitude at plasma surface [T]
c	speed of light in vacuo [m/s]
$\delta = \Im(k)$	skin depth [1/m]
ε_0	permittivity of free space [F/m]
E_0	electric field amplitude at plasma surface [V/m]
E_{dr}	driving electric field amplitude [V/m]
$\phi,\ \chi$	angle or phase [rad]
f	plasma frequency [Hz]
F_p	ponderomotive force [N]
$F^{\pm} = \frac{1}{2}(E \pm cB)$	forward and backward moving EM wave [V/m]
$H_0 = B_0/\mu_0$	auxiliary magnetic field amplitude at plasma surface [A/m]
J	electric current [A]
κ	arbitrary coefficient of effective conductivity
k	complex wave number [1/m]
$K = \Re(k)$	real component of wave number [1/m]
λ	electron mean free path [m]
L_{pl}	length of plasma chamber [m]
μ_0	permeability of free space [H/m]
m_e	electron mass [kg]
M	total number of mesh points
ν	electron-neutral collision frequency [rad/s]
n_e	electron density [$1/m^3$]
N	total number of particles
p	pressure [kg/m^2] or number of processors
P	power [W] or probability
q	electric charge [C]
ρ	charge density [C/m^3]
$\rho_L = m_e v/eB$	electron Larmor radius [m]
R_n	random value n
$R_{\parallel}$	reflection coefficient
σ	conductivity [$1/\Omega{\cdot}m$] or cross section [m^2]
S	Poynting flux [$J/m^2{\cdot}s$] and shape function
T_e	electron temperature [eV]
u	fluid velocity [m/s]
v	velocity [m/s]
$v_{Te} = \sqrt{eT_e/m_e}$	electron thermal velocity [m/s]
$\omega_{pe}^2 = n_e e^2/m_e\varepsilon_0$	electron plasma frequency [rad/s]
$\omega = 2\pi f$	driving frequency [rad/s]
z	position coordinate in plasma normal to surface [m]
$\zeta_0 = \sqrt{\mu_0/\varepsilon_0}$	impedance of free space [Ω]

Chapter 1

Introduction

1.1 Inductively Coupled Plasmas

An inductively coupled plasma (ICP) is formed when an electromagnetic (EM) wave travels through a low-density gas. This is usually accomplished by winding a coil around a vacuum chamber to form a solenoid, or forming a stove-top element shape and placing it at the end of the cylinder (Fig. 1.1). A radio frequency (RF) alternating current is excited in the coil, which creates an EM wave that propagates through the cylinder, ionizing the gas and creating a plasma.

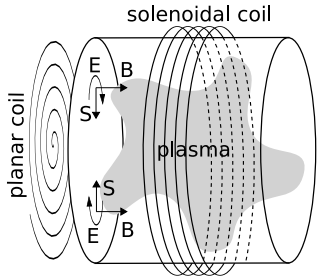

Figure 1.1: ICP antenna configurations can be solenoidal or planar. An axial magnetic field B and azimuthal electric field E are induced with the wave S travelling towards the centre of the device.

ICP devices are commonly used for microscale etching and deposition, spectroscopy, and low-maintenance lighting (Fig. 1.2). Due to the fact that the energizing coil is not in direct contact with the plasma, as are the electrodes in a capacitively coupled plasma, electron densities as high as $n_e = 10^{18}\,\mathrm{m}^{-3}$ can be achieved. These densities enable a similarly high etch rate in semiconductor processing applications and rapid sample ionization in spectrochemical analysis. The absence of electrodes also limits contact with the chamber walls, reducing sample contamination and increasing device longevity. All applications benefit from the low power input necessary to drive the RF coil.

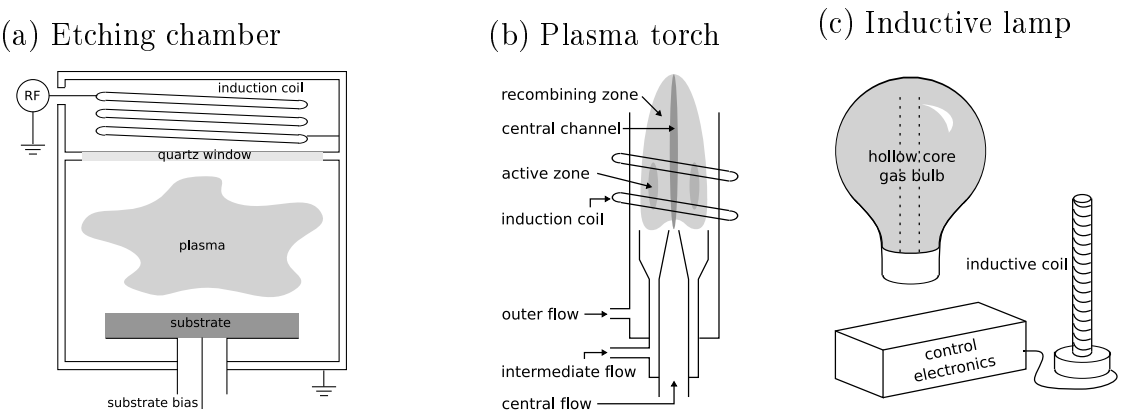

Figure 1.2: ICP devices in various applications. (a) Etching chamber: The plasma ions strike the substrate, etching grooves in the material. (b) Plasma torch: The sample gas is pumped through the inner channel, the plasma gas through the intermediate channel, and the insulating gas through the outer channel. (c) Inductive lamp: A solenoid is placed in the core of a closed bulb of gas. The lifetime of these lamps is limited only by that of the electronics.

Once the plasma forms, it inhibits propagation of all radiation below the electron plasma frequency$\omega_{pe} = (n_e e^2/m_e\varepsilon_0)^{1/2}$, where n_e is the electron density, e is the elementary charge, m_e is the electron mass, and ε_0 is the permittivity of free space (Fig. 1.3). Since ICP devices usually host high electron densities, the EM wave almost certainly becomes evanescent upon entry into the plasma, creating a skin layer which essentially acts as a counter-winding to the coil. The wave is partially reflected, with the absorbed energy accelerating the particles in the skin layer. In the presence of the magnetic field, the force is directed parallel to the wave and is termed the ponderomotive force (PMF). If there is a mechanism to diffuse this motion, the plasma is ultimately heated by the wave.

1.1.1 Nonlocal Effects

In the absence of a strong magnetic field, three frequencies govern the interaction of a wave with a plasma: the driving frequency f, the collision frequency ν, and the electron transit frequency, or rate at which a thermal electron traverses the skin layer, given by v_{Te}/δ, where v_{Te} is the electron thermal velocity and δ is the skin depth. If the driving frequency is high ($\omega \gg \nu$, v_{Te}/δ), electrons do not move far during a single wave period and experience a local electric field. If the collision

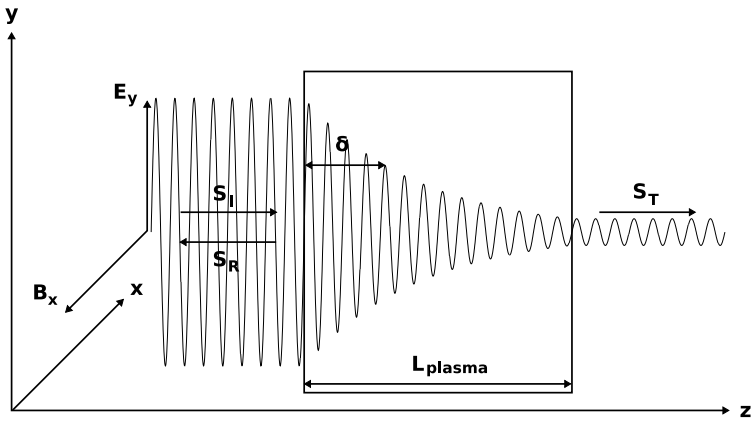

Figure 1.3: Schematic diagram of an electromagnetic wave penetrating a plasma in one-dimension. The fields on the left side of the plasma are a superposition of the incoming S_I and reflected S_R waves, while on the right side is only the transmitted wave S_T. Inside the plasma, the waves in the skin layer decay at a rate of $1/\delta$.

frequency is high ($\nu \gg \omega$, v_{Te}/δ), friction prevents the electrons from moving in a directed manner, so they again experience a local electric field.

If the electron transit frequency is high ($v_{Te}/\delta \gg \omega$, ν), then the electrons sample the spatial variance of the electric field by moving through the skin layer. This causes the electric current to be nonlocally dependent on the fields, and may result in an electron distribution that is non-Maxwellian and skin fields that do not decay exponentially. Linear theories can accommodate this complication, but only if the magnetic field is weak. Should a nonlocal plasma experience a low frequency wave, the magnetic field will produce non-linear trajectories which must be tracked via computer simulation.

1.1.2 Nonlinear Effects

ICP devices are used for many applications, and while the underlying physical equations are known to be Maxwell's equations and particle kinetic equations, the effects and subtleties that arise from a simple set of initial and boundary conditions are not fully understood. Even the most complex analytical models for low pressure ICP [16, 17] use linear models for simplicity. The process of linearization disregards two real effects, the magnetic field and the longitudinal electric field. The magnetic field comes from the EM wave and causes the particle trajectories to be curved, while the longitudinal electric field occurs because the electrons are accelerated more quickly in response to the ponderomotive force (PMF) than the ions. This creates a charge

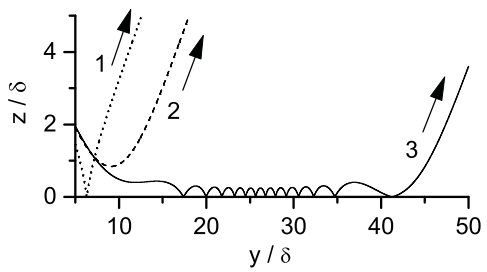

Figure 1.4: Example trajectories of an electron passing through the skin layer [19]. Entry angle, speed, and field strength affect the curvature of the paths. Electron 1 follows a nearly straight trajectory and is spectrally reflected from the boundary. Electron 2 is reflected by the fields before reaching the boundary. Electron 3 is temporarily trapped in the skin layer due to curvature combined with spectral reflection.

separation normal to the skin layer that is counteracted by the longitudinal field. These effects are difficult to analyze, therefore a quasilinear approximation is made that all particles travel in straight lines and are not accelerated normal to the surface, so that they spend a predictable length of time in the skin layer. Then nonlinear quantities, such as the PMF, are determined from the prescribed currents and the calculated fields.

In reality, the path a particle takes through the skin layer is curved and highly dependent on its speed, direction of flight, and strength of the fields (Fig. 1.4), especially at low frequency, $\omega \ll v_{Te}/\delta$. Therefore, the skin depth, surface impedance, and ponderomotive force cannot be properly calculated in the low frequency regime, where they show significant deviation from predicted linear behaviour. Computer simulations do not suffer limitations from nonlinearities, and can provide us with a more detailed picture of the phenomena that occur under all conditions. It is desirable to explore the plasma parameter space over as large a range as possible in order to observe different behaviour regimes. By starting with a simple model and gradually adding complexities such as magnetic fields, mobile ions, and collisions with neutral atoms, it should be possible to explain the cause of the resulting physical effects.

1.2 Objectives

The purpose of this thesis was to discover the regimes of behaviour of a ICP plasma, identify their range in observable parameters, and explain the origin of each regime.

simulation mode ⇒ regimes observed ⇓	linear collisionless	linear collisional	nonlinear collisionless	nonlinear collisional
local collisionless	present	not run	present	present
local collisional	absent	not run	absent	absent
anomalous skin effect	present	not run	present	present
nonlinear	absent	not run	present	absent

Table 1.1: Comparison of the mode of simulation versus the behavioural regimes observed in the plasma. Linear collisional mode was tested successfully, but not used for any production runs. Simulated collision rates were too low for the plasma to reach the local collisional regime.

Linear theories describe three regimes: the local collisionless regime when the driving frequency is high, the local collisional regime when the collision frequency is high, and the anomalous skin effect regime when the electron transit frequency is high. An additional regime is identified in this work; the nonlinear regime is present when the driving wave frequency is low and amplitude is high.

To determine the origin of these regimes, the linearity can be forced and collisions can be activated for various simulation runs. This gives 4 different modes to test: linear collisionless, linear collisional, nonlinear collisional, and nonlinear collisional. (In the context of modes, collisional does not necessarily mean collisions dominate, but just that they are present.) To artificially force linearity in the simulation, the particles ignore all forces normal to the skin layer, so the magnetic and longitudinal electric fields have no effect. Table 1.1 gives a basic summary of which regimes are present in each simulation mode.

1.3 Project Overview

This project can be divided into two stages. The first was to develop software tools required to simulate the plasma and verify the accuracy of the simulation. Two preexisting programs were used to create a self-consistent ICP simulation, both written by D. Sydorenko [19] at the University of Saskatchewan for his Ph.D. thesis. One was a serial particle-in-cell (PIC) simulation of ICP without collisions, while the other was a PIC simulation of a Hall thruster with a versatile collision algorithm that ran on multiple CPUs in parallel. Using these as a basis, a parallel PIC simulation of ICP was produced that was capable of performing electron-neutral collisions.

Before the nonlinear dynamics could be investigated, the simulation had to cor-

roborate the results of linear theories [16, 17, 25]. Several programs were written to perform the analytical computations, and the results compared to thsoe generated by the PIC program in linear mode. The primary test of the collision algorithm was to reproduce the results of one of the first ICP simulations [20]. For non-collisional plasmas, the program accuracy was tested by comparing the output with that of the original serial ICP program. After the consistency tests were completed, the nonlinear behaviour of the plasma was studied.

The second stage of the project was the methodical investigation of the parameter space over driving wave frequency and amplitude, plasma temperature, ion mobility, and collision frequency. The driving wave frequency and amplitude are most easily varied in experiments, and so they were scanned most extensively from $f = 1$ to 100 MHz and $E_{dr} = 10^3$ to 10^5 V/m, respectively. The driving wave amplitude is the controllable parameter, but is not physically observed, because it is mostly cancelled by the reflected wave coming from the plasma. At the plasma surface, the electric field varies between $E_0 = 0.1$ and 10^4 V/m. Once the general features and regime boundaries in frequency-amplitude space were determined in great detail at a single temperature with immobile ions, a more selective range was scanned at other temperatures and with mobile ions of varying masses.

1.4 Thesis Outline

Chapter 2 describes theoretical models of ICP. Formulae for the skin effect, surface impedance, and ponderomotive force in the local, anomalous, and nonlinear regimes are developed. Computed results from each of the linear theories are compared.

Chapter 3 gives a detailed description of the self-consistent PIC simulation that is used. It covers the one-dimensional advective model, the sequence of operations for the PIC algorithm, the quasineutral approximation used as a substitute for Poisson's equation, the Monte Carlo collision algorithm, and the parallelization method and its efficiency.

Chapter 4 shows all the pertinent results from the simulation. The different regimes are identified and the modifications to the plasma in the nonlinear regime are described.

Chapter 5 discusses the effect of temperature on the regime boundary. Independent calculations of the characteristic path length through the skin layer are presented to further explain the nonlinear results. The chapter closes with open questions and the conclusion.

Chapter 2

Theory

There are many measurable phenomena that occur in ICP; however, the primary concern is for three particular features: (1) the skin layer, (2) the surface impedance, and (3) the ponderomotive force.

2.1 Skin Layer

When an EM wave with frequency lower than the plasma frequency ($2\pi f = \omega < \omega_{pe}$) penetrates a plasma, it becomes evanescent. Electromagnetic plane waves in a conductor have the form:

$$\mathbf{E}(z,t) = \mathbf{E}_0 e^{i(kz-\omega t)}, \qquad \mathbf{B}(z,t) = \mathbf{B}_0 e^{i(kz-\omega t)}, \tag{2.1}$$

where E_0 is the electron field amplitude, B_0 is the magnetic field amplitude, k is the complex wave number, z is the distance into the plasma, ω is the wave frequency, and t is the time. In the case of an evanescent wave, the fields are attenuated with a decay rate $1/\delta = \Im(k)$, where δ is the skin depth. Letting $K = \Re(k)$ represent the oscillatory component of the wave number, the fields become:

$$\mathbf{E}(z,t) = \mathbf{E}_0 e^{-z/\delta} e^{i(Kz-\omega t)}, \qquad \mathbf{B}(z,t) = \mathbf{B}_0 e^{-z/\delta} e^{i(Kz-\omega t)}. \tag{2.2}$$

By assuming a local plasma with stationary ions, an ICP can be sufficiently described by Maxwell's equations[1], the electron continuity equation, and the electron fluid equation of motion:

[1] For our purposes, Ampere's law and Faraday's law are sufficient. Taking the divergence of each gives $\nabla \cdot (\partial \mathbf{B}/\partial t) = 0$ and $\nabla \cdot (\varepsilon_0 \partial \mathbf{E}/\partial t) = -\nabla \cdot \mathbf{J} = \partial \rho / \partial t$. Therefore, $\nabla \cdot \mathbf{B} = 0$ and $\nabla \cdot \mathbf{E} = \rho/\varepsilon_0$ are always satisfied since they hold for an initially homogeneous, neutral plasma.

$$
\begin{aligned}
\nabla \times \mathbf{E} &= -\frac{\partial \mathbf{B}}{\partial t}, \\
\nabla \times \mathbf{B} &= \mu_0 \mathbf{J} + \mu_0 \varepsilon_0 \frac{\partial \mathbf{E}}{\partial t}, \\
0 &= \nabla \cdot (n_e \mathbf{u}) + \frac{\partial n_e}{\partial t}, \\
m_e \frac{d\mathbf{u}}{dt} &= -e(\mathbf{E} + \mathbf{u} \times \mathbf{B}) - \nabla p - m_e \nu \mathbf{u},
\end{aligned} \tag{2.3}
$$

where $\mathbf{J}$ is the electric current, μ_0 and ε_0 are the permeability and permittivity of free space, respectively, n_e is the electron density, m_e is the electron mass, $\mathbf{u}$ is the electron fluid velocity, and ν is the total electron collision rate.

To find the skin depth, a number of simplifications can make the problem more tractable. The pressure term can be dropped if the plasma is homogeneous and isothermal. A linear approximation allows each mode to be treated independently, and therefore, all fields can be assumed to vary as $e^{i(kz-\omega t)}$. Since the antenna is being driven at a low frequency relative to the electron plasma frequency $\omega \ll \omega_{pe}$, the displacement current is insignificant and the electrons are able to keep up with the changes in the externally applied fields. To illustrate the basic properties, one can replace the equations with a linearized one-dimensional model along the $\hat{z}$ axis:

$$
\begin{aligned}
-i\omega m_e \mathbf{u} &= -e\mathbf{E} - m_e \nu \mathbf{u}, \\
\nabla \times \mathbf{E} &= i\omega \mathbf{B}, \\
\nabla \times \mathbf{B} &= \mu_0 \mathbf{J}.
\end{aligned} \tag{2.4}
$$

To find the dispersion equation $k(\omega)$, Maxwell's equations are combined:

$$
\begin{aligned}
i\omega\mu_0 \mathbf{J} &= \nabla \times (\nabla \times \mathbf{E}) \\
&= \nabla(\nabla \cdot \mathbf{E}) - \nabla^2 \mathbf{E} \\
&= -\mathbf{k}(\mathbf{k} \cdot \mathbf{E}) + k^2 \mathbf{E}.
\end{aligned} \tag{2.5}
$$

Since the EM wave is transverse in a quasineutral plasma, $\mathbf{k} \cdot \mathbf{E} = 0$, the electric current is given by:

$$
\mathbf{J} = -ne\mathbf{u} = \frac{-ik^2}{\omega\mu_0}\mathbf{E}. \tag{2.6}
$$

The electron fluid equation (Eq. 2.3d) provides an alternative relation between the

electron velocity and electric field:

$$\mathbf{u} = \frac{-ie\mathbf{E}}{m_e(\omega + i\nu)}. \tag{2.7}$$

Comparing these two equations, one arrives at the dispersion relation:

$$c^2k^2 = \frac{-\omega_{pe}^2\omega}{\omega + i\nu}, \tag{2.8}$$

where $\omega_{pe} = (n_e e^2/m_e\varepsilon_0)^{1/2}$ is the plasma frequency. Letting $\nu \ll \omega$ gives the local skin depth for a collisionless plasma

$$\delta_c = \frac{1}{\Im(k)} = \frac{c}{\omega_{pe}}. \tag{2.9}$$

To find the collisional skin depth, it is convenient to introduce the following variables

$$\epsilon \equiv \tan^{-1}\frac{\nu}{\omega} \qquad a \equiv \frac{\nu}{\omega} \qquad \delta_0 \equiv \frac{c}{\omega_{pe}}(1+a^2)^{1/4}, \tag{2.10}$$

following Chen [2]. This makes the dispersion relation

$$k^2 = \frac{-\omega_{pe}^2/c^2}{1+ia} = \frac{-1}{\delta_0^2}\exp(-i\epsilon). \tag{2.11}$$

Then the local collisional skin depth is found to be:

$$\delta_s = \frac{1}{\Im(k)} = \delta_0\sec(\epsilon/2) = \delta_c\sqrt{\frac{2(1+a^2)}{1+(1+a^2)^{1/2}}}. \tag{2.12}$$

2.1.1 Anomalous Skin Effect

When eliminating the magnetic field from the Maxwell equations, it is implicitly assumed that the current is dependent only on the local electric field. However, if the mean free path of a thermal electron is long compared to the skin depth, $\lambda \gg \delta$, then most electrons will sample a varying electric field between infrequent collisions, making the current nonlocal. Therefore, when an ICP is run at low pressure, the observed skin depth is actually much longer than the local collisional value.

While this effect is described by the dispersion function of an EM wave in a plasma, it was unexplained at the time of its discovery in metals by London [12]. In order to explain the anomaly in the observed skin depth, Pippard [14] pointed

out that electrons that spend little time in the skin layer should not contribute significantly to the skin current because they have insufficient time to be accelerated by the skin field. Therefore, only those that enter at angles less than δ/λ (the ratio of skin depth to mean free path) make "effective" contributions to the current before colliding and returning to the plasma bulk. By assuming that the plasma conductivity is determined only by the effective electrons, the skin depth can be found as in Ref. [7], starting with the effective conductivity:

$$\sigma_{eff} = (\delta/\lambda)\kappa\sigma. \tag{2.13}$$

The equation for the electric current is transformed from $\mathbf{J} = \sigma\mathbf{E}$ to

$$\mathbf{J} = (\delta/\lambda)\kappa\sigma\mathbf{E}, \tag{2.14}$$

where κ is a numerical constant whose value is dependent on the electron distribution function. Weibel [24] finds it to be $\kappa = \sqrt{\pi}$ for a Maxwellian distribution. Comparing this to Eq. 2.6, the skin depth resulting from this new conductivity can be determined,

$$\frac{\delta}{\lambda}\kappa\sigma = \frac{ik^2}{\omega\mu_0}. \tag{2.15}$$

By assuming that $\delta = 1/|k|$, the anomalous skin depth is approximated as:

$$\delta_a = \left(\frac{\lambda}{\omega\mu_0\kappa\sigma}\right)^{1/3}. \tag{2.16}$$

This expression is the asymptotic limit of the rigorous treatment [15] at low frequencies, and therefore is invalid in the local regime at high frequencies. In the collisionless case, the effective mean free path is the distance a thermal particle moves in one period, $\lambda = v_T/\omega$. Since the conductivity is $\sigma = ne^2/m_e\omega$, the skin depth can be rewritten

$$\delta_a = \left(\frac{v_T}{\sqrt{\pi}}\frac{c^2}{\omega_{pe}^2\omega}\right)^{1/3}. \tag{2.17}$$

This form is more commonly found in the literature [15].

2.1.2 Nonlinear Skin Depth

While the previous theories ignore the magnetic field term in the electron fluid equation of motion (2.3d), it would be desirable to estimate the skin depth in the presence

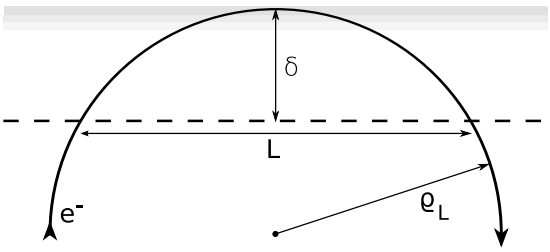

Figure 2.1: To estimate the skin depth δ in the presence of a magnetic field, an electron is assumed to travel on a circular path with Larmor radius ρ_L through the skin layer. The distance traveled inside the skin layer L replaces the electron mean free path when determining the conductivity.

of a magnetic field. Therefore, we develop a simple theory that follows the treatment of the anomalous skin depth. Assuming a strong magnetic field arising from a low frequency EM wave ($\omega \ll 1/\delta \implies B \gg E$) and weak collisions ($\rho_L \gg \lambda$), the electrons should pass through the skin layer along nearly circular, uninterrupted orbits. Since the electrons will be most strongly affected by the fields at the plasma boundary, the orbital radius is set to be tangent to the boundary, and chosen to have a constant Larmor radius ρ_L corresponding to the magnetic field strength at the edge, where it is maximum. Then the characteristic length is the distance the electron travels inside the skin layer (Fig. 2.1), approximated by $L_{nl} \simeq \sqrt{\rho_L \delta}$ when the Larmor radius is much greater than the skin depth, $\delta \ll \rho_L = m_e v_T / eB_0$. The characteristic length is then substituted for the mean free path in the effective conductivity (Eq. 2.13):

$$\sigma_{eff} = (\delta / L_{nl}) \kappa \sigma, \tag{2.18}$$

where σ is the conductivity and κ is now an unknown parameter. Starting with the relation

$$i\omega\mu_0\sigma_{eff} = \frac{1}{\delta^2}, \tag{2.19}$$

the collisionless nonlinear skin depth is found to be

$$\delta_{nl} = \left(\frac{c^4}{\omega_{pe}^4} \frac{\rho_L}{\pi} \right)^{1/5} = \left(\frac{m_e^3 v_T}{\pi \mu_0^2 n_e^2 e^5 B_0} \right)^{1/5}. \tag{2.20}$$

Unlike the anomalous skin depth, this expression is independent of driving frequency, but changes slowly with the driving amplitude. It is found empirically (Sec. 4.3) that the nonlinear skin depth is only valid when it falls between the anomalous skin depth and local skin depth, $\delta_c < \delta_{nl} < \delta_a$.

2.1.3 Skin Fields

When dropping the pressure term from Eq. 2.3 for the skin depth, temperature dependence is also eliminated. Without thermal motion, particles only respond to their local conditions, and the fields within the skin layer of a semi-infinite, homogeneous plasma decay exponentially. At finite temperatures, electrons travel about the skin layer influencing the current at each location with a velocity accumulated from the fields along their past trajectory. This nonlocal response causes the fields to decay non-exponentially and even non-monotonically [24, 7, 2], sometimes to the point of reversing (Fig. 2.2). The field-reversal can even cause negative power absorption by that section of the plasma [4, 21].

It is difficult to define the skin depth with precision in a finite-temperature plasma, as the definition is equivocal when the fields are not exponential, as in Fig. 2.2. However, thermal effects are most evident deep inside the plasma where the amplitude is orders of magnitude weaker than at the surface, and at the surface exponential decay is actually a reasonable approximation (Fig. 2.2). Therefore the skin depth can be calculated as

$$\delta = \left. \frac{\Re(E_y(z))}{\Re(E_y'(z))} \right|_{z=0}, \tag{2.21}$$

where $z = 0$ indicates the field amplitudes are acquired from the plasma boundary.

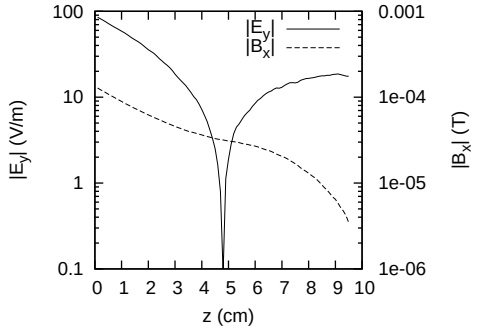

Figure 2.2: Example of the maximum electric and magnetic field amplitudes throughout the skin layer. The electric field reverses direction 5 cm inside the plasma. Envelopes acquired from a nonlinear simulation with immobile ions and plasma parameters $f = 4$ MHz, $E_{dr} = 2 \times 10^5$ V/m, $n_e = 10^{17}$ m^{-3}, $L_{pl} = 10$ cm, and $T_e = 10$ eV.

In the local case when the temperature is low, $\nu \gg v_T/\delta$ or $\omega \gg v_T/\delta$, the conductivity becomes a linear relation and Ohm's law, $\mathbf{J} = \sigma\mathbf{E}$, is valid. Then a

simple approximation [20] to the shape of the fields can be found with Maxwell's equations (2.4) to arrive at the Helmholtz equation

$$\frac{d^2E_y}{dz^2} + i\omega\sigma\mu_0 E_y = 0. \tag{2.22}$$

With the boundary condition that the electric field disappears at $z = L$, the solution is

$$E_{y,local}(z) = \mu_0 \frac{\omega}{k} \frac{\sinh(k(L_{pl} - z))}{\cosh(kL_{pl})}, \tag{2.23}$$

where k is given by the dispersion relation in Eq. 2.8. Plugging this back into Faraday's law gives the corresponding magnetic field

$$B_{x,local}(z) = -i\mu_0 \frac{\cosh(k(L_{pl} - z))}{\cosh(kL_{pl})}. \tag{2.24}$$

There is no temperature dependence in these equations, and therefore, they apply only to the local case of high-frequency, low-temperature, or highly collisional plasmas. In the anomalous skin effect regime, they are only useful as a first approximation.

For the general case that includes thermal and collisionless plasmas, Weibel [24] and Shaing [15] developed linear models to self-consistently determine the skin fields of a semi-infinite plasma. Shaing also describes a plasma in a finite-sized container of length L_{pl} [16], in which the magnetic field and electron current are found to have complex amplitudes given by:

$$\begin{aligned} E_y(z) &= -\frac{2U}{L_{pl}} \sum_{n=0}^{\infty} \frac{\cos(\phi_n z)}{\phi_n^2 - \frac{\omega^2}{c^2} + i\alpha L_{pl} k_n(a)}, \\ B_x(z) &= -i\frac{2U}{\omega L_{pl}} \sum_{n=0}^{\infty} \frac{\phi_n \sin(\phi_n z)}{\phi_n^2 - \frac{\omega^2}{c^2} + i\alpha L_{pl} k_n(a)}, \end{aligned} \tag{2.25}$$

where $\phi_n = (2n+1)\pi/2L_{pl}$, $\alpha = 8\sqrt{\pi} n_e e^2 \omega/(m_e v_T c^2)$, $U = -dE_y/dz|_{z\to 0^+}$ is the rate of change of the electric field near the plasma boundary, and $k_n(a)$ describes the rate at which electrons cross the device relative to the driving frequency. When the collision frequency is independent of the electron energy, it equals:

$$k_n(a) = \int_0^\infty dy \exp(-y^2) \left[aL + \frac{(-1)^n (n+\frac{1}{2})\pi y}{\sinh(aL_{pl}/y)} \right] \Bigg/ \left\{ (aL)^2 + \left[\left(n + \frac{1}{2} \right) \pi y \right]^2 \right\}. \tag{2.26}$$

The first term in square brackets describes the wave-particle resonance in a semi-

infinite system, while the second describes the resonance between the driving frequency and the wall bounce frequency.

A difficulty arises when computing Shaing's equations, as the expression for the magnetic field is numerically unstable, and suffers rapid oscillation when $z \ll L_{pl}$. This is because the magnetic field is not continuous when the system is extended to an infinite periodic system. Yoon *et al.* [25] propose an alternate formulation which avoids this problem. The fields are given by

$$\begin{aligned} E_y(z) &= B_0 \left[\frac{e_0}{2} + \sum_{n=1}^{\infty} e_n \cos(k_n z) \right], \\ B_x(z) &= B_0 \left[1 + \frac{z}{L_{pl}} \left(\frac{\xi_2}{\xi_1} - 1 \right) + \sum_{n=1}^{\infty} b_n \sin(k_n z) \right], \end{aligned} \tag{2.27}$$

where $k_n = n\pi/L_{pl}$ is the wave number and the dimensionless summation terms are

$$\begin{aligned} e_n &= -\frac{i\omega}{c} \frac{2}{L_{pl}} \left(1 - (-1)^n \frac{\xi_2}{\xi_1} \right) Q_n, \\ b_n &= \frac{2}{L_{pl}} \left(1 - (-1)^n \frac{\xi_2}{\xi_1} \right) (k_n Q_n - k_n^{-1}), \end{aligned} \tag{2.28}$$

$$\xi_1 = \frac{Q_0}{2} + \sum_{n=1}^{\infty} Q_n, \qquad \xi_2 = \frac{Q_0}{2} + \sum_{n=1}^{\infty} (-1)^n Q_n. \tag{2.29}$$

The auxiliary functions,

$$Q_n \equiv \left(k_n^2 - i\mu_0 \omega \sqrt{2\pi} \sigma_n \right)^{-1}, \tag{2.30}$$

are used so that the summation converges rapidly as $Q_n \sim k_n^{-2} \sim n^{-2}$. The auxiliary function contains the term σ_n, which is the Fourier component of the conductivity for an infinite homogeneous plasma

$$\sigma_n = \begin{cases} \frac{i}{\sqrt{\pi}} \frac{\varepsilon_0 \omega_{pe}}{2\lambda_D} \frac{v_{Te}}{\omega + i\nu}, & k = 0, \\ \frac{-i}{\sqrt{\pi}} \frac{\varepsilon_0 \omega_{pe}}{2\lambda_D} \frac{1}{|k|} Z_p \left(\frac{\omega + i\nu}{|k_n| v_{Te}} \right), & k \neq 0, \end{cases} \tag{2.31}$$

where $\lambda_D = \sqrt{\varepsilon_0 T_e / ne}$ is the Debye length, k with no subscript is the wavenumber defined as before Eq. 2.8, and Z_p is the plasma dispersion function [3]:

$$Z_p(p) = \frac{1}{\sqrt{\pi}} \int_{-\infty}^{\infty} \frac{\exp(-x^2)}{x - p} dx, \tag{2.32}$$

which is defined for $\Im(p) > 0$. While there are many steps involved, this algorithm has the added benefit of being computationally faster than Shaing's technique because there are no integrals to evaluate.

Fields from each theory for different collision frequencies are shown in Fig. 2.3. The electric fields coincide with one another quite well at high collision frequencies, but show small differences at low frequencies. However, the magnetic fields show large differences in both form and magnitude. One can see clearly that the magnetic field from Shaing's theory shows poor convergence. Note how each theory exhibits some fields that decay nonmonotonically.

2.2 Surface Impedance

The power absorption of a plasma must be known, in order to maximize the heating efficiency of the RF antenna. It is determined by integrating the Poynting flux over a surface that encloses the plasma

$$P_{total} = \int_S (\mathbf{E} \times \mathbf{H}^\star) \cdot d\mathbf{A}. \tag{2.33}$$

Assuming the plasma is semi-infinite and the EM wave penetrates the boundary normal to the surface, the average power transmitted per unit area is $P = \frac{1}{2} E_y H_x$. Hence, the fields must be calculated at some point outside the plasma to find the absorbed power, but only the incoming wave amplitude is known: $E_{in} = E_{dr}$ and $H_{in} = E_{dr}/\mu_0 c$. The actual fields will prove to be less than this, because the Poynting flux from the reflected wave will reduce the net flux into the plasma.

Faraday's law shows that there is a factor relating the transverse magnetic to the transverse electric field,

$$H_x(x) = \frac{\omega \mu_0}{k} E_y(x). \tag{2.34}$$

However, the wave vector k takes different values inside and outside the plasma, and therefore, so does the magnetic field. The fields inside the plasma are not of interest, and they can be ignored if the boundary boundary condition at the interface is known. The factor at the boundary is defined as the surface impedance $\zeta = \omega\mu_0/k = \sqrt{\mu/\varepsilon} = E_y(0)/H_x(0)$ [8]. Employing this value, the power transmitted per unit area can be rewritten as

$$P = \frac{1}{2} \Re(\zeta) \left| H_x(0) \right|^2. \tag{2.35}$$

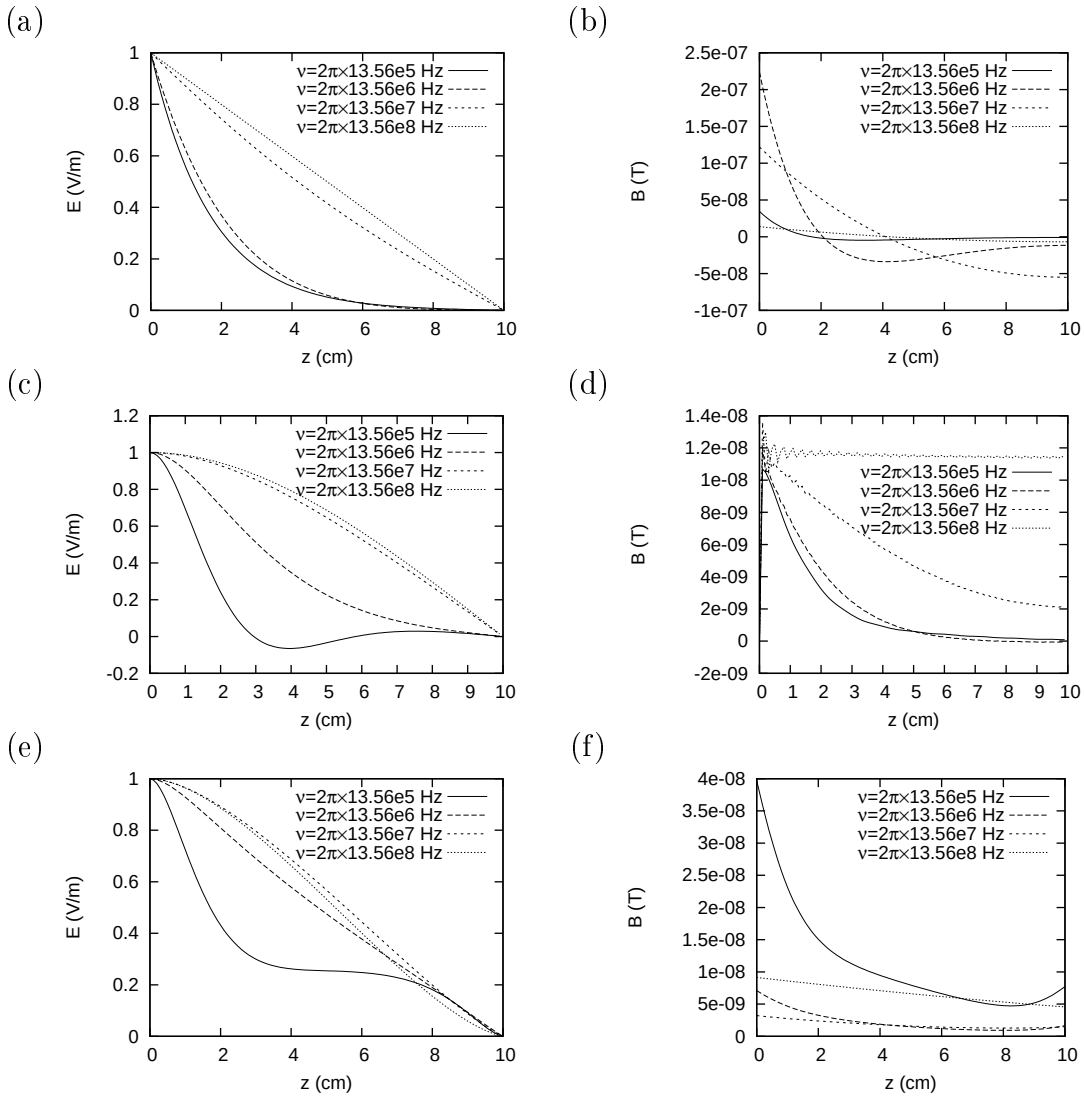

Figure 2.3: The amplitude profiles of the electric and magnetic fields in the skin layer at a driving frequency of $f = 13.56$ MHz and various collision frequencies ν as given by different theories: (a,b) the local approximation, Eqs. 2.23 and 2.24; (c,d) the theory of Shaing *et al.* [16], Eq. 2.25; (e,f) and the theory of Yoon *et al.* [25], Eq. 2.27.

The real component of the surface impedance is proportional to the power flux into the plasma. Highly conductive materials have large permittivities and strongly reflect EM waves, so the surface impedance is correspondingly small. The imaginary component gives the reactive power or phase shift between the fields. Since the skin depth is defined by $\delta = 1/\Im(k)$, the imaginary part of the surface impedance can be found via the relationship

$$\zeta = \frac{\omega\mu_0}{k} \implies \Im(\zeta) = \omega\mu_0\delta. \tag{2.36}$$

Due to the fact that a plasma acts similar to a conductor, the surface impedance is proportional to the energy absorbed by the plasma, which can provide an alternative, more reliable source of measurement. The permittivity of a plasma is a very large negative value $\varepsilon \sim -\infty$, which makes the surface impedance very small, $|\zeta| \ll |\zeta_0|$, where $\zeta_0 = \sqrt{\mu_0/\varepsilon_0}$ is the impedance of free space. The reflection coefficient for an EM wave crossing the interface between materials normal to the surface is given by

$$R_\parallel = \left|\frac{\zeta_0 - \zeta}{\zeta_0 + \zeta}\right|^2. \tag{2.37}$$

Under the condition of a small surface impedance, most of the wave is reflected and the absorbed power is linearly related to the surface impedance,

$$P_{absorbed} = \left(1 - R_\parallel\right) P_{input} \simeq 4\Re\left(\frac{\zeta}{\zeta_0}\right) P_{input}. \tag{2.38}$$

Since this treatment has assumed a semi-infinite plasma, the energy that would pass completely through a finite-length plasma and exit the far side has been ignored. For evanescent waves in most typical ICP devices, this is justified, as the fraction of energy that traverses even a few centimetres of plasma is fleetingly small.

In the approximation of a collisional plasma, Eqs. 2.23 and 2.24 are combined to arrive at the local approximation to the surface impedance

$$\zeta_{local} = i\mu_0\frac{\omega}{k}\tanh(kL). \tag{2.39}$$

Based on the theory of the anomalous skin effect in metals, Weibel solved the problem of a semi-infinite thermal plasma with electrons that are specularly reflected at the plasma boundary by substituting the Fermi electron distribution with a Maxwellian.

His linear analysis [7] shows the surface impedance to be

$$\zeta = -\frac{i\omega\lambda_{eff}}{\pi c}\int_{-\infty}^{\infty}\frac{dk}{k^2+\Lambda Z_p(is/k)/k}, \tag{2.40}$$

where $\lambda_{eff} = v_T/\sqrt{\nu^2+\omega^2}$ is the effective mean free path, $s = \lambda_{eff}(\nu+i\omega)/v_T$, and Λ is the nonlocality parameter, given as

$$\Lambda = \left(\frac{\omega_{pe}v_{Te}}{c}\right)^2\frac{\omega}{(\nu^2+\omega^2)^{3/2}} \simeq \frac{\lambda_{eff}^2}{\delta^2}. \tag{2.41}$$

Of course, no physical device is semi-infinite, as is assumed in these previous treatments. A finite length plasma was first simulated by Turner [20], which confirmed that the local theory was not accurate for a collisionless plasma. Shaing's finite system (Eq. 2.25) gives a result for the surface impedance,

$$\zeta = i\zeta_0\frac{\omega}{c}\frac{2}{L}\sum_{n=0}^{\infty}\frac{1}{\phi_n^2 - \frac{\omega^2}{c^2} + i\alpha L k_n(a)}, \tag{2.42}$$

that closely matches Turner's data. In the local limit, the wall bounce terms become insignificant and the equations reproduce Weibel's result. In the cold, collisional limit, it is:

$$\zeta_{collisional} = \zeta_0\frac{\sqrt{i\omega\nu}}{\omega_{pe}}, \tag{2.43}$$

while in the anomalous skin effect regime, the expression is approximated by

$$\zeta_a = \zeta_0\frac{\omega}{c}\frac{2}{3}\left(\frac{1}{\sqrt{3}}+i\right)\left(\frac{v_T}{\sqrt{\pi}}\frac{c^2}{\omega_{pe}^2\omega}\right)^{1/3}. \tag{2.44}$$

Yoon's field equations can also be used to produce a formula for the impedance

$$\zeta = i\zeta_0\frac{\omega}{c}\frac{2}{L}\left[\frac{\xi_2^2}{\xi_1} - \xi_1\right]. \tag{2.45}$$

These linear expressions are compared in Fig. 2.4, while the effect of collisions on surface impedance at different frequencies as determined by Shaing's theory are shown in Fig. 2.5. When collisions are present, the impedance $\Re(\zeta)$, and hence power absorption, increases around the region where $\omega \sim 2\pi\nu$.

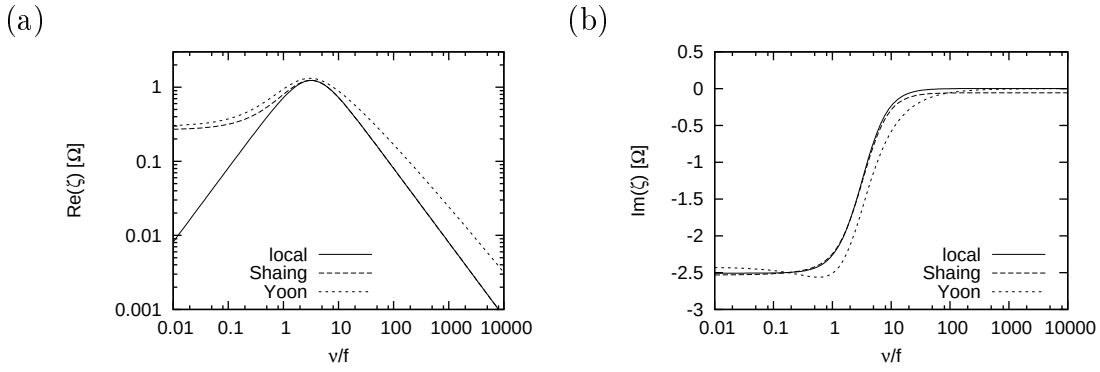

Figure 2.4: The surface impedance, as derived from the theories by Shaing and Yoon and the local approximation, for a wave of frequency $f = 13.56$ MHz entering a plasma of length $L_{pl} = 4$ cm, density $n_e = 10^{17}\,\mathrm{m}^{-3}$, and temperature $T_e = 5$ eV.

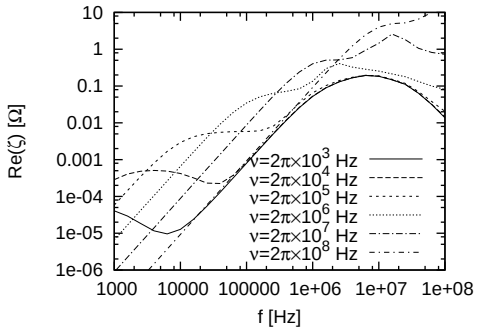

Figure 2.5: The surface impedance, as found with Eq. 2.42, for various driving frequencies f and collision frequencies ν in a plasma of length $L_{pl} = 10$ cm, density $n_e = 10^{17}\,\mathrm{m}^{-3}$, and temperature $T_e = 1$ eV. The case of no collisions coincides with the minimum for all collision frequencies.

2.3 Ponderomotive Force

When an EM wave impinges on a plasma, the fields act upon the electrons via the Lorentz force. The force depends on the speed and direction of flight of each charged particle, and therefore, does not have a consistent effect on individual electrons. However, collectively, the plasma experiences a radiation pressure from the wave. Averaging the Lorentz force over a full wave cycle and over all particles gives the ponderomotive force (PMF) or Miller force, which points in the direction of wave travel and pushes the plasma particles away from the antenna.

Since the electric component of the Lorentz force averages to zero over a wave cycle, the PMF can be found with just the magnetic contribution

$$\mathbf{F}_p = \frac{1}{2}\Re(\mathbf{J} \times \mathbf{B}^\star). \tag{2.46}$$

The PMF is a second-order effect and cannot be described by linear theories self-consistently; it depends upon the magnetic field, but the particles are not influenced by the magnetic field in the linear approximation. Since the force is independent of particle mass, the electrons are accelerated much more quickly than the ions. This separates the electrons and ions and sets up a longitudinal electric field between them, which further compromises the accuracy of linear descriptions.

2.3.1 Cold-Plasma Approximation

Despite the fact that the PMF is defined as an average over all particles, it can be analyzed by considering the motion of a single particle. Since this approach omits the electron energy distribution function, it precludes the possibility of describing a thermal plasma, but it is useful as a first step. The force is found by solving the electron equation of motion in oscillating electric and magnetic fields:

$$\begin{aligned} m\frac{d\mathbf{v}}{dt} &= -e(\mathbf{E} + \mathbf{v} \times \mathbf{B}) - m\nu\mathbf{v}, \\ \mathbf{E}^{(1)} &= \mathbf{E}_s \cos\omega t, \\ \mathbf{B}^{(1)} &= -\frac{1}{\omega}\nabla \times \mathbf{E}_s \sin\omega t. \end{aligned} \tag{2.47}$$

In first-order, the Lorentz force disappears, so the velocity of the electron and its displacement are:

$$\begin{aligned} \mathbf{v}^{(1)} &= -\frac{e}{m\omega}\mathbf{E}_s(1+a^2)^{-1}(\sin\omega t + a\cos\omega t), \\ \mathbf{dr}^{(1)} &= \frac{e}{m\omega^2}\mathbf{E}_s(1+a^2)^{-1}(\cos\omega t - a\sin\omega t), \end{aligned} \tag{2.48}$$

where $a = 2\pi\nu/\omega$ is the collisionality parameter. Expanding $\mathbf{E}(\mathbf{r})$ around $\mathbf{r}_0$, the second-order equation of motion is

$$m\frac{d\mathbf{v}^{(2)}}{dt} = -e\left[(\mathbf{dr}^{(1)}\cdot\nabla)\mathbf{E}^{(1)} + \mathbf{v}^{(1)}\times\mathbf{B}^{(1)})\right] - m\nu\mathbf{v}^{(2)}, \tag{2.49}$$

which, after plugging in first-order values, produces:

$$\begin{aligned} \frac{d\mathbf{v}^{(2)}}{dt} + \nu\mathbf{v}^{(2)} &= -\frac{e^2}{m^2\omega^2}\frac{1}{1+a^2}\left[(\cos^2\omega t - a\sin\omega t\cos\omega t)\mathbf{E}_s\cdot\nabla\mathbf{E}_s\right. \\ &\quad \left.+(\sin^2\omega t + a\sin\omega t\cos\omega t)\mathbf{E}_s\times(\nabla\times\mathbf{E}_s)\right]. \end{aligned} \tag{2.50}$$

The final term can be modified by:

$$\mathbf{E}_s\times(\nabla\times\mathbf{E}_s) = \frac{1}{2}\nabla\mathbf{E}_s^2 - (\mathbf{E}_s\cdot\nabla)\mathbf{E}_s, \tag{2.51}$$

but in a transverse wave, the intensity varies in the direction of the wave vector, which is perpendicular to the electric field polarization. Therefore, the terms involving the gradient of the electric field disappear and the ponderomotive force takes the form

$$\mathbf{F}_p = -\frac{\omega_{pe}^2}{\omega^2}\frac{1}{1+a^2}\frac{\varepsilon_0}{2}\nabla\left\langle E^2\right\rangle(1-\cos 2\omega t + a\sin 2\omega t). \tag{2.52}$$

in a plasma with no thermal motion. By assuming a skin layer that decays exponentially in the z-direction, the force is

$$\mathbf{F}_p = \frac{\omega_{pe}^2}{\omega^2+\nu^2}\frac{\varepsilon_0 E_0^2}{2\delta}\hat{z}, \tag{2.53}$$

when time-averaged over a wave cycle.

2.3.2 Thermal Plasma Linear Approximation

The added complexity of a thermal distribution of electron velocities requires that the equations be linearized and the magnetic field be ignored by the particles. The

solution of the PMF under these conditions has been accomplished both with prescribed field profiles and self-consistent fields (Self-consistent in that the fields are affected by the plasma, but the plasma is affected by the fields only via linear processes. This excludes the magnetic and longitudinal electric fields.)

Smolyakov *et al.* [17] assume that the electric and magnetic fields in the skin layer decay exponentially. This approximation is justified because non-monotonic behaviour usually takes place deep inside the plasma where the fields are smaller. Therefore, the approximation should be accurate where the PMF is large. The field profiles are defined as:

$$\begin{aligned} E_y(z,t) &= E_0 \exp(-\gamma z) \exp(-i\omega t), \\ B_x(z,t) &= \frac{i\gamma}{\omega} E_0 \exp(-\gamma z) \exp(-i\omega t), \end{aligned} \tag{2.54}$$

where E_0 is the field amplitude at the plasma boundary, $\gamma = 1/\delta - i\xi$ is the complex longitudinal wave number, δ is the skin depth, and ξ determines the energy flux into the plasma. The calculated PMF is found to be:

$$F_p = \frac{\omega_p^2}{2\omega} \varepsilon_0 E_0^2 \exp\left(-\frac{2z}{\delta}\right) \Re\left\{ i \frac{\gamma^*}{\gamma v_T} \left[Z(-is) - \exp(\gamma z) G(\gamma z, s) \right] \right\}, \tag{2.55}$$

where Z is the plasma dispersion function (Eq. 2.32), $s = (\omega + i2\pi\nu)/\gamma v_T$, and:

$$G(\gamma z, s) = \frac{2}{\sqrt{\pi}} \int_0^\infty \frac{t \exp(i\gamma z s/t - t^2)}{t^2 + s^2} dt. \tag{2.56}$$

This expression recovers the cold-plasma approximation when $s \to \infty$. Assuming small energy flux, the limit in the anomalous skin effect regime is found by replacing the skin depth δ by the particle excursion over the wave period $\delta_T = v_T/\sqrt{\pi}\omega$.

The alternative approach is to use Yoon's model in which the fields are calculated self-consistently. The electric current density is given by

$$J_y(z) = B_0 \left[\frac{j_0}{2} + \sum_{n=1}^{\infty} j_n \cos(k_n z) \right], \tag{2.57}$$

where the summation terms are $j_n = \sqrt{2\pi}\sigma_n e_n$ with the use of Eq. 2.28 and 2.31. Combined with the magnetic field, one can use the Eq. 2.46 to find the ponderomotive force at all positions in the plasma for different collision frequencies (Fig. 2.6). The values predicted by local approximation and Yoon agree with one another for high collision rates, but Smolyakov's theory takes different starting assumptions

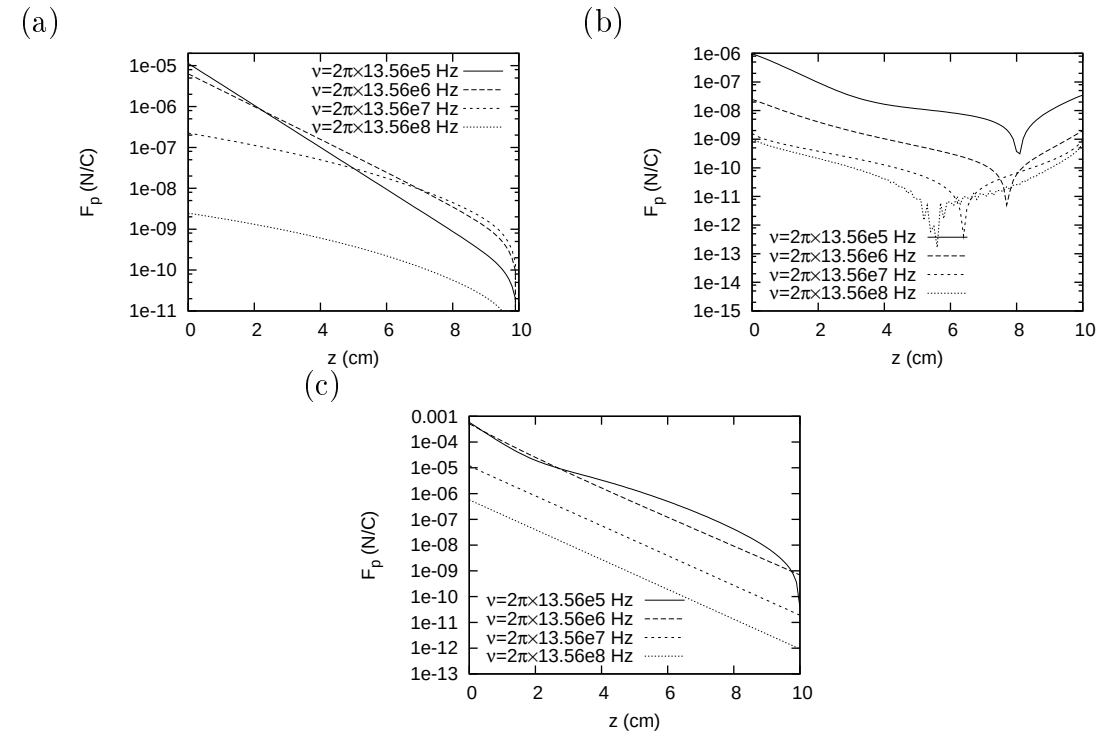

Figure 2.6: The strength of the ponderomotive force profile throughout the skin layer at a driving frequency of $f = 13.56$ MHz and various collision frequencies ν as calculated via the following theories: (a) the local approximation, Eqs. 2.23 and 2.24; (b) the theory of Yoon *et al.*, by plugging Eq. 2.27 into Eq. 2.46; (c) and the theory of Smolyakov *et al.*, Eq. 2.55.

than the other two, and so, arrives at a slightly larger PMF.

2.3.3 Nonlinear Ponderomotive Force

Using Amperes law, Eq. 2.46 can be reformed to describe the ponderomotive force as

$$\begin{aligned} \mathbf{F}_p &= \frac{1}{2\mu_0}\Re\{(\nabla \times \mathbf{B}) \times \mathbf{B}^\star\} \\ &= \frac{-1}{2\mu_0}\Re\{\frac{1}{2}\nabla B^2 + (\mathbf{B}\cdot\nabla)\mathbf{B}^\star\}. \end{aligned} \tag{2.58}$$

Since the magnetic field is transverse, the second term drops out. Assuming an exponential profile, the expression becomes

$$F_p = \frac{B^2}{2\mu_0\delta}. \tag{2.59}$$

This expression should hold true for all values of the skin depth. For the case when the magnetic field is strong, such that $\rho \ll \lambda$, the estimate for the nonlinear skin depth is plugged in to arrive at

$$F_p = \frac{B_0^2}{2\mu_0}\left(\frac{\pi\mu_0^2 n e^3 B_0}{m_e^2 v_T}\right)^{1/5}. \tag{2.60}$$

This result, as well as the other asymptotic behaviour presented in this chapter is shown in Table 2.1.

Regime	Local, Collisionless	Local, Collisional	Anomalous	Nonlinear
Conditions	$f \gg \nu, v_T/\delta$	$\nu \gg f, v_T/\delta$	$v_T/\delta \gg \nu, f$	$\lambda \gg \rho_L \gg \delta$
Skin Depth δ	$\frac{c}{\omega_{pe}}$	$\frac{c}{\omega_{pe}}\sqrt{\frac{2\nu}{\omega}}$	$\left(\frac{v_T}{\sqrt{\pi}}\frac{c^2}{\omega_{pe}^2\omega}\right)^{1/3}$	$\left(\frac{m_e^3 v_T}{\pi\mu_0^2 n_e^2 e^5 B_0}\right)^{1/5}$
Surface Impedance ζ	$i\zeta_0$	$\zeta_0\sqrt{\frac{i\omega\nu}{\omega_{pe}}}$	$\zeta_0\frac{\omega}{c}\frac{2}{3}\left(\frac{1}{\sqrt{3}}+i\right)\delta_a$	
Power Absorption P	0	$H_0^2\sqrt{\frac{8\omega\nu}{\omega_{pe}}}$	$H_0^2\frac{\zeta_0}{3\sqrt{3}}\frac{\omega}{c}\delta_a$	
Ponderomotive Force F_p	$\frac{\omega_{pe}^2}{\omega^2}\frac{\varepsilon_0 E_0^2}{2\delta_c}$	$\frac{\omega_{pe}^2}{\nu^2}\frac{\varepsilon_0 E_0^2}{2\delta_\nu}$	$\frac{\sqrt{\pi}}{2}\frac{\omega_{pe}^2}{\omega}\frac{\varepsilon_0 E_0^2}{v_T}$	$\frac{B_0^2}{2\mu_0\delta_{nl}}$

Table 2.1: Summary of asymptotic behaviour in each regime for all theoretical results presented in this chapter.

Chapter 3

Self-Consistent Simulation

The PIC program used to generate the data for this thesis is based on the original serial version written by D. Sydorenko [19] at the University of Saskatchewan for his Ph.D. thesis. It was parallelized using the Message Passing Interface (MPI), a common parallelization library, to run on multiple processors simultaneously and tested to ensure the results corroborated those generated using the serial program (Fig. 4.8d). Collision algorithms from another program were grafted in, with changes made to permit interoperability. Most calculations were performed on the Westgrid cluster Matrix at the University of Alberta.

3.1 1d2v Electromagnetic Model

The description of ICP in plane slab geometry is a standard textbook subject [1]. The following advective algorithm was developed by Dawson and Langdon. Assuming that the impinging EM wave is traveling normal to the surface of the plasma, and denoting that direction as $\hat{z}$, the plasma model is taken to be homogeneous in the $\hat{x}$ and $\hat{y}$ directions. Maxwell's equations can then be simplified to

$$\frac{\partial B_x}{\partial z} = \mu_0 J_y + \mu_0 \varepsilon_0 \frac{\partial E_y}{\partial t}, \tag{3.1}$$

$$\frac{\partial E_y}{\partial z} = \frac{\partial B_x}{\partial t}. \tag{3.2}$$

Because there is no electric field in the $\hat{x}$ direction, and no magnetic field in the $\hat{y}$ and $\hat{z}$ directions, only the $\hat{y}$ and $\hat{z}$ components of velocity need to be recorded for each particle. Therefore, the model is "1d2v," signifying the number of position and velocity variables under consideration, in this case: z, v_y, and v_z (Fig. 3.1).

Adding and subtracting the Maxwell equations permits the introduction of a quantity for waves travelling forwards (F^+) versus those travelling backwards (F^-)

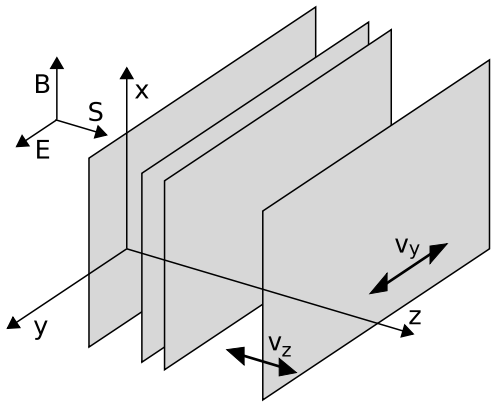

Figure 3.1: Schematic of the motion of particle slabs in the simulation. Each slab is homogeneous in the x and y directions. No forces act on the slabs in the x direction.

$$F_y^{\pm} = \frac{1}{2}(E_y \pm cB_x). \tag{3.3}$$

Maxwell's equations become

$$\left(\frac{\partial}{\partial t} \pm c\frac{\partial}{\partial z}\right) F_y^{\pm} = -\frac{1}{2}\frac{J_y}{\varepsilon_0}. \tag{3.4}$$

The net Poynting flux at any point can then be found easily as:

$$S = \frac{1}{\zeta_0}\left[(F^+)^2 - (F^-)^2\right]. \tag{3.5}$$

Boundary conditions are based on the assumption that the plasma is surrounded by vacuum, with a wave impinging from the left. In the vacuum, the magnitude of the magnetic field is related to that of the electric field by Faraday's law, so that $E_y = cB_x$. By plugging this into the identity for F^+, the left boundary condition becomes:

$$F^+(z = 0, t) = E_{dr}\sin(ft) = cB_{dr}\sin(\omega t), \tag{3.6}$$

while at the right boundary, there is no incoming wave:

$$F^-(z = L_{pl}, t) = 0. \tag{3.7}$$

The advantage of recording $F^{\pm}$ instead of the actual electric and magnetic fields is that in the absence of electric current propagation simply requires shifting the values of F^+ to the right and those of F^- to the left. By setting the time step $\Delta t = \Delta z/c$, the shift becomes exactly one mesh element. This is computationally simple, and

since Δz is on the order of millimetres, the time step is on the order of the period of plasma oscillations ($c/\Delta z \sim \omega_{pe}$). This ensures that the driving and collision frequencies are well resolved ($c/\Delta z \gg \omega, \nu$). The only disadvantage is the large number of steps required to complete each run.

3.2 Particle-in-Cell Algorithm

The obvious method of modelling the dynamics of an N-body system is via a particle-particle algorithm, where each particle interacts with all others, as it does in reality. However, this requires computation time on the order of $\mathcal{O}(N^2)$ and hence, limits the number of particles that can be handled feasibly by the simulation. It is much more efficient to project all the particle properties $\mathcal{O}(N)$ onto an M-celled grid on the z-axis, find the resulting force fields on the mesh $\mathcal{O}(M)$, and interpolate those forces back to the particles $\mathcal{O}(N)$. Such a technique is called a particle-mesh (PM) or particle-in-cell (PIC) algorithm and is particularly useful when electromagnetic fields are involved, since the grid is already required to store the spatial dependence of those fields.

The combined use of particles in phase-space with a spatial grid requires a method for projecting the charge from the particles to the grid and interpolating the fields from the grid to the particles. To accomplish this, the particles are interpreted as finite-sized clouds, with the shape of the cloud determining the order of interpolation, and therefore, called the shape factor (Fig 3.3). The shape factor is used to calculate the mesh charge as

$$\rho^n(Z_j) \equiv \sum_i q_i S(Z_j - z_i^n), \tag{3.8}$$

where ρ^n is the charge density at time n, Z_j is the position of mesh point j, q_i is the charge of particle i, and z_i^n is the position of particle i at time n. Similar equations are used to find other plasma properties, except for the temperature, which involves an extra smoothing step for the sake of the quasineutral electric field algorithm.

Commonly used shape factors (Fig. 3.3a) include the zero-order nearest grid point (NGP), first-order cloud-in-cell (CIC), and second-order quadratic spline functions. The NGP function gives very rough mesh densities because it moves the entire charge of each particle to the nearest point on the mesh. The CIC function puts a linear weighting between the points that surround the particle. This is not much more computationally taxing than NGP, but gives much smoother data (Fig. 3.3b), which is the reason it is used in the program. The quadratic splines function distributes

the charge over the nearest three points. It creates a very smooth mesh result, but requires many more calculations to perform.

The major source of error in PIC simulations is discrete particle noise [13]. It can be reduced by using a higher order shape factor or increasing the number of particles occupying each cell. With a large number of particles per cell, each one will represent less charge and cause a smaller fluctuation when passing between cells. The statistical error approximately $\sqrt{M/N}$, inversely related to the number of particles per cell. Typically, runs were performed with 10000 particles per cell, limiting discrete particle noise to less than 1%.

Other sources of numerical error are the finite mesh size and finite time step. However, these are much less significant than particle noise in a PIC simulation. The mesh size must be larger than the Debye length to avoid instabilities, but once this condition is satisfied, it is more beneficial to increase the particle number than increase the grid resolution when computational resources are limited [9]. Likewise, the discretization of the time step produces little error, so long as the step size is small enough to resolve plasma oscillations and thermal motion, as described by [11],

$$\Delta t \ll \frac{\pi}{\omega_{pe} + \pi v_T M/L_{pl}}. \tag{3.9}$$

As described before, the time step is on the order of the plasma oscillation period, but not much less as this equation indicates is necessary. However, the quasineutral approximation is employed to produce an algorithm, described in Section 3.3, which underdamps the plasma oscillations and hence, eliminates the need to resolve such high frequencies [5].

3.2.1 Sequence of a Time Step

For this description of system evolution, it is useful to follow along in Fig. 3.2. To find the state of the particle system at the $(n+1)^{th}$ time step, the particle positions z_i^n and the transverse electric and magnetic fields E_y^n, B_x^n at the current time step n, as well as the particle velocities $v_i^{n-1/2}$ at the $(n-\frac{1}{2})^{th}$ half-step are necessary. The positions and velocities are half a time step out of sync so that each can be advanced using the time-averaged value of the other. This leapfrog method increases the stability and accuracy of the evolution because it is time-symmetric, and therefore, conserves energy.

Step (1) involves projecting the particle moments onto the mesh. The properties of each particle are weighted among the nearby cells by a shape factor to find the

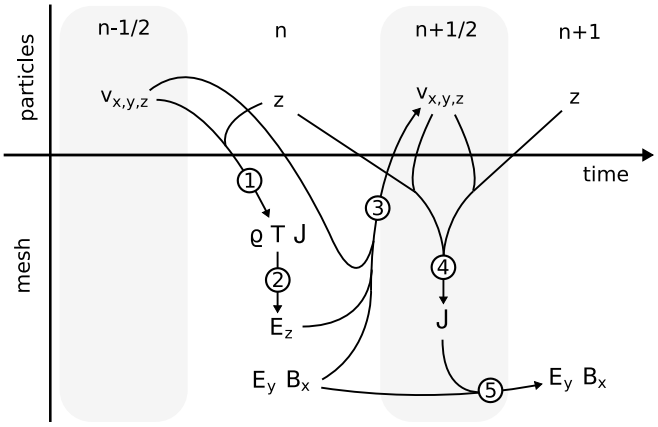

Figure 3.2: A pictorial representation of the steps required to advance the simulated plasma one increment in time. All quantities shown above the horizontal line are particle properties. These include only the velocity $v_{x,y,z}$ and position z. The quantities below the line are mesh properties, which include the plasma density ρ, temperature T, and current J, longitudinal electric field E_z, and transverse fields E_y and B_x. A description of each numbered step can be found in Section 3.2.1. A linear simulation does not include Step (2).

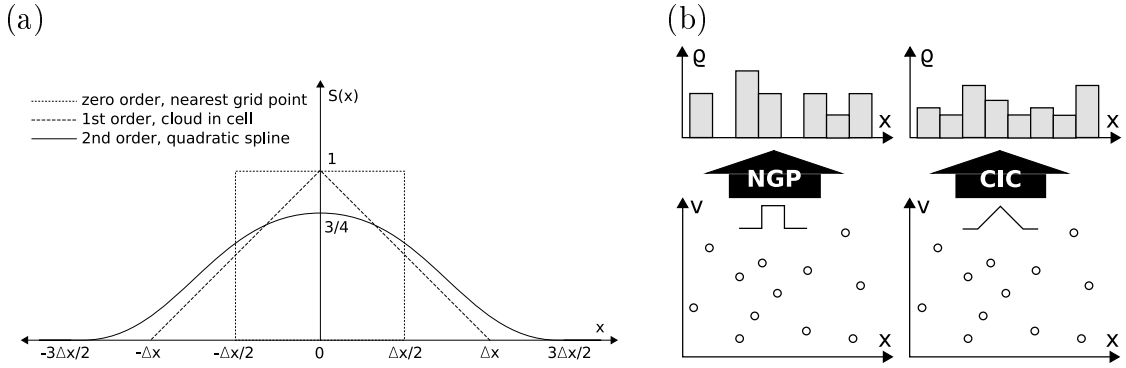

Figure 3.3: (a) Three basic shape factors for projecting particles onto the mesh. Each function is normalized so that $\int S(x)dx = 1$. (b) An example of the improvement of the first-order cloud-in-cell (CIC) shape factor over the zero-order nearest grid point (NGP) in terms of function smoothness.

charge density, temperature, and current on the mesh.

Step (2) uses the mesh values to find the longitudinal electric field. In a charged plasma or one driven at high-frequency, Poisson's equation is used to calculate the field from the charge density. However, when the plasma is quasineutral, it is highly susceptible to the stochastic noise from the PIC simulation. Therefore, a quasineutral approximation, described in Sec. 3.3, is used. It reduces noise and is computationally faster than Poisson's equation by avoiding the slow process of solving coupled equations.

Step (3) interpolates the fields on the mesh, E_y, E_z, and B_x, to the particles by the same shape factor as was used previously. Then each particle is accelerated via the Lorentz force. The most efficient methods for performing the acceleration calculation are described in Birdsall and Langdon 4-3 [1], but all are mathematically equivalent to the centred-difference form

$$\frac{\mathbf{v}_i^{n+1/2} - \mathbf{v}_i^{n-1/2}}{\Delta t} = \frac{q_i}{m_i}\left[\mathbf{E}_i + \frac{\mathbf{v}_i^{n+1/2} + \mathbf{v}_i^{n-1/2}}{2} \times \mathbf{B}_i\right]. \tag{3.10}$$

If there are electron-neutral collisions, they are performed at the end of this step to randomize the recently calculated velocities.

Step (4) moves each particle based on its new velocity by:

$$z_i^{n+1} = z_i^n + v_z^{n+1/2}\Delta t. \tag{3.11}$$

If a particle hits an edge of the plasma, it is specularly reflected.

Step (5) uses both the old and new positions as well as the new velocities and evaluates the electric current centred both in space between cells, and in time at step $(n + \frac{1}{2})$,

$$\begin{aligned} J_y^{n+1/2}(Z_{j+1/2}) \quad &= \tfrac{1}{4}\textstyle\sum_i q_i v_i^{n+1/2} \quad [S(Z_j - z_i^n) + S(Z_{j+1} - z_i^n) + \\ &\qquad S(Z_j - z_i^{n+1}) + S(Z_{j+1} - z_i^{n+1})\big]. \end{aligned} \tag{3.12}$$

Step (6), the last step, updates the transverse electric fields to the time $(n + 1)$. However, besides simple propagation of the left-going wave moving left and the right-going wave moving right, the plasma currents modify the amplitude. The currents are recorded at positions directly between the mesh cells, so that when the EM fields cross them to reach the next cell, the left- and right-going waves are influenced by

the same amount

$$\mathbf{F}_y^{\pm}(Z_j) = \mathbf{F}_y^{\pm}(Z_{j\mp1}) - \frac{1}{2\varepsilon_0}\mathbf{J}_y^{n-1/2}(Z_{j\mp1/2}). \tag{3.13}$$

Once this step is complete, the cycle begins again.

3.3 Quasineutral Approximation

The PMF accelerates the electrons much more rapidly than the ions, causing a charge separation in the longitudinal direction. To maintain plasma neutrality, a longitudinal electric field that points into the plasma arises to compensate. Ordinarily, the longitudinal field is calculated using Poisson's equation, but if a plasma is quasineutral, as is the case when it is driven by a low-frequency wave, the density fluctuations are small and mostly stochastic, due to the limited number of particles in a numerical simulation. Such behaviour produces a noisy longitudinal electric field. An alternative technique has been developed empirically by Joyce *et al.* [5] that begins with the electron fluid equation of momentum conservation:

$$m_e n_e \frac{d\mathbf{u}}{dt} = -en_e\left(\mathbf{E} + \mathbf{u}\times\mathbf{B}\right) - \nabla\cdot\mathbf{P}, \tag{3.14}$$

where m_e, n_e, and $\mathbf{u}$ are the electron mass, density, and fluid velocity, and $\mathbf{P}$ is the pressure tensor. By assuming the electron energy distribution function is isotropic, the pressure can be replaced by the temperature.

$$\mathbf{P} = \int d^3v\, m_e \mathbf{v}\mathbf{v} f(\mathbf{x},\mathbf{v},t) \equiv n_e T_e(\mathbf{x},t)\mathbf{I}. \tag{3.15}$$

For the one-dimensional problem, only the $\hat{z}$ component is necessary:

$$m_e n_e \frac{du_z}{dt} = -en_e(E_z - u_y B_x) - \frac{\partial}{\partial z}(n_e T_{ez}). \tag{3.16}$$

Solving this for the electric field gives:

$$E_z = -\frac{J_y B_x}{en_e} - \frac{1}{en_e}\frac{\partial}{\partial z}(n_e T_{ez}) - \frac{m_e}{n_e}\frac{du_z}{dt}, \tag{3.17}$$

where the current is $J_y = -en_e u_y$. The first two terms represent the ambipolar electric field, while the last inertial term is responsible for maintaining quasineutrality. The problem is that the last term is negligible compared to the others, so the electron acceleration is essentially random. To fix this, the electric field is modified

to artificially increase the charge separation perceived by the electrons:

$$\begin{aligned} E_z &= -\frac{J_y B_x}{e n_e} - \frac{1}{e n_e}\frac{\partial}{\partial z}(n_e T_{ez}) + \left[\frac{1}{e n_i}\frac{\partial}{\partial z}(n_i T_{ez}) - \frac{1}{e n_i}\frac{\partial}{\partial z}(n_i T_{ez})\right] - \frac{m_e}{n_e}\frac{du_z}{dt} \\ &= -\frac{J_y B_x}{e n_e} - \frac{1}{e n_i}\frac{\partial}{\partial z}(n_i T_{ez}) + \left[\frac{1}{e n_i}\frac{\partial}{\partial z}(n_i T_{ez}) - \frac{1}{e n_e}\frac{\partial}{\partial z}(n_e T_{ez}) - \frac{m_e}{n_e}\frac{du_z}{dt}\right]. \end{aligned}$$

Letting the sum in the brackets be equal to zero, the new electric field will cause the electrons to accelerate towards regions where the ion density is higher than the electron density:

$$m_e \frac{du_z}{dt} = T_{ez}\frac{\partial}{\partial z}\ln\left(\frac{n_i}{n_e}\right). \tag{3.18}$$

Because the acceleration has been greatly increased, the electrons will oscillate around regions of positive charge density. This under-relaxation means that there is no need to time-centre the calculation, but both the temperature input and the resultant electric field must be smoothed to damp out these high-frequency oscillations. This scheme is purported to have excellent stability and energy conservation properties.

3.4 Collisions

Electrons and ion species interact with one another via the Coulomb force, but an ICP is only weakly ionized, so there is a large population of neutral atoms interspersed with the plasma. While the interaction distance is much shorter, the charged particles are capable of colliding with the neutrals by inducing a dipole. The most common collisions in an argon ICP include electron-neutral and ion-neutral elastic scattering, ion-neutral charge exchange, excitation, ionization, and recombination. Because the total number of charged particles is a constant in this program, the ionization and recombination are not possible because they involve the creation or destruction of an electron-ion pair.

While all the reactions that conserve the number of charged particles are implemented, for simplicity only the electron-neutral elastic scattering with a constant collision frequency is employed. Because the neutral atoms are not tracked, the method for imitating electron-neutral collisions [23] involves using a Monte Carlo algorithm to randomly choose electrons and change their velocity. The program is implemented with multiple possibilities for scattering distribution as well as collision frequency dependence.

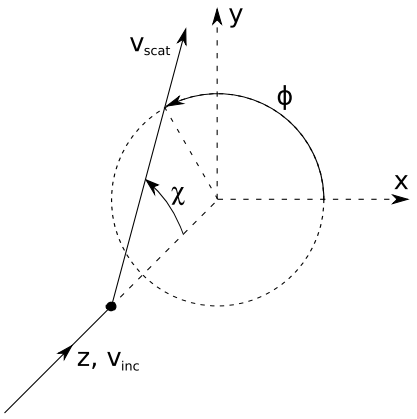

Figure 3.4: In the centre of mass frame, an electron comes in from the lower-left and collides with a stationary neutral atom (black dot). The electron is deflected by angle χ from its original path. The direction of deflection ϕ is isotropic.

3.4.1 Scattering Distribution

For a single collision, the centre of mass coordinate system is oriented so that the incoming electron is travelling in the z-direction with velocity $\mathbf{v}_{inc}$, as shown in Fig. 3.4. Then the angle of deflection with the imaginary neutral atom is given by:

$$\cos\chi = \frac{\mathbf{v}_{scat}\cdot\mathbf{v}_{inc}}{v_{scat}v_{inc}} = \frac{\mathbf{v}_{scat}}{v_{scat}}\cdot\hat{z} \tag{3.19}$$

and the azimuthal direction of scatter ϕ is:

$$\cos\phi = \frac{\mathbf{v}_{scat}}{v_{scat}}\cdot\hat{x}. \tag{3.20}$$

Assuming spherically symmetric atoms, a colliding electron has an equal probability of being scattered in any perpendicular direction. Therefore, the ϕ is uniformly distributed on the interval $[0, 2\pi]$, which can be calculated as:

$$\phi = 2\pi R_1, \tag{3.21}$$

where R_1 is a randomly generated number in the range $[0, 1]$.

To determine the deflection angle, there are two distributions currently implemented. The first is simply isotropic, which is useful for diagnostics, while the other is energy dependent, which is most physically accurate. The calculation of the deflection angle in the isotropic case is identical to that of the azimuthal angle, except

that a separate random variable $R_2 \in [0, 1]$ is used to calculate

$$\chi = \pi R_2. \tag{3.22}$$

The physically motivated distribution is based on the screened Coulomb scattering of an electron off an induced dipole [18], which is dependent on the relative speed of the electron and atom. A large interaction energy should result in a small forward scattering angle, while a small energy should produce an isotropic distribution. An approximate differential cross section that gives this behavior is

$$\frac{\sigma(\varepsilon, \chi)}{\sigma(\varepsilon)} = \frac{\varepsilon}{4\pi \left[1 + \varepsilon \sin^2(\chi/2)\right] \ln(1 + \varepsilon)}. \tag{3.23}$$

where $\varepsilon = m_e v^2 / 2\varepsilon_1$ is the kinetic energy of the incident electron relative a reference electron with kinetic energy $\varepsilon_1 = 1$ eV. To randomly generate the angle χ from this equation, one must solve

$$R_2 = \frac{\int_0^\chi \sigma(\varepsilon, \chi) \sin\chi d\chi}{\int_0^\pi \sigma(\varepsilon, \chi) \sin\chi d\chi} \tag{3.24}$$

to arrive at

$$\cos\chi = \frac{2 + \varepsilon - 2(1 + \varepsilon)^{R_2}}{\varepsilon}. \tag{3.25}$$

Note that the scattering angle is again dependent on $R_2 \in [0, 1]$. Once the direction angle ϕ and scattering angle χ have been selected, they are then used to find the scattering vector

$$\mathbf{v}_{scat} = v_{inc} \left(\hat{\mathbf{z}} \cos\chi + \hat{\mathbf{y}} \sin\chi \sin\phi + \hat{\mathbf{x}} \sin\chi \cos\phi\right), \tag{3.26}$$

which can then be converted back to lab coordinates.

Since the mass of the electron m is much less than the neutral atom M, there is not much energy transferred in the collision. The change, rarely more than 1%, is given by

$$\Delta\varepsilon = \frac{2m}{M}(1 - \cos\chi). \tag{3.27}$$

This is used to scale the scattered velocity after its direction has been determined.

To test whether the scattering cross-section is calculated properly, a beam is initialized with all the electrons travelling at a uniform velocity in the z-direction. The beam starts with energy ε and velocity $v_z = 1$, so that all velocities are normalized by the initial beam velocity. Forcing all particles to scatter in one time step will

cause the velocity distribution to transform with the differential cross section as:

$$f(\mathbf{v}) = \frac{\sigma(\varepsilon,\chi)}{\sigma(\varepsilon)}\delta(v-1), \tag{3.28}$$

where $\delta(x)$ is the Dirac delta function. To achieve a distribution that is testable with the program output, the scattered distribution must be projected into the v_y and v_z dimensions:

$$f(v_z) = \int_{-\infty}^{\infty} dv_x \int_{-\infty}^{\infty} dv_y \frac{\sigma(\varepsilon,\chi)}{\sigma(\varepsilon)}\delta\left(\sqrt{v_x^2+v_y^2+v_z^2}-1\right). \tag{3.29}$$

For the isotropic case, the differential cross section is

$$\frac{\sigma(\varepsilon,\chi)}{\sigma(\varepsilon)} = \frac{1}{2\pi^2\sin\chi} = \frac{1}{2\pi^2\sqrt{1-v_z^2}}, \tag{3.30}$$

where the second formulation makes use of the definition $v_z = \cos\chi$. Projecting to v_z is most simple in cylindrical coordinates, where $v_\rho^2 = v_x^2 + v_y^2$, so that:

$$f(v_z) = \int_0^{2\pi} d\phi \int_0^{\infty} dv_\rho v_\rho \frac{\delta\left(\sqrt{v_\rho^2+v_z^2}-1\right)}{2\pi^2\sqrt{1-v_z^2}}. \tag{3.31}$$

To solve an integral with a complicated Dirac delta function, the following formula must be employed

$$\int_{-\infty}^{\infty} f(t)\delta[g(t)]dt = \sum_i \frac{f(t_i)}{\left|\frac{dg}{dt}\right|_{t=t_i}}, \tag{3.32}$$

where the t_i are all the zeros of the function $g(t)$. The final solution becomes

$$f(v_z) = \frac{1}{\pi}\left[\frac{v_\rho}{\sqrt{1-v_z^2}}\frac{\sqrt{v_\rho^2+v_z^2}}{v_\rho}\right]_{v_\rho=\sqrt{1-v_z^2}} = \frac{1}{\pi\sqrt{1-v_z^2}}. \tag{3.33}$$

The solution to the v_y projection requires elliptic functions, so the solution is provided,

$$f(v_y) = \frac{4}{\pi^2|v_y|}K\left(\frac{\sqrt{v_y^2-1}}{|v_y|}\right), \tag{3.34}$$

where $K(k) = \int_0^1 dt/(\sqrt{1-t^2}\sqrt{1-k^2t^2})$. Plots (a) and (b) in Fig. 3.5 show that results match these functions identically after one scattering. The second scattering shows that the distribution continues to approach uniform after further collisions.

Performing the same calculations on the screened Coulomb distribution Eq. 3.23,

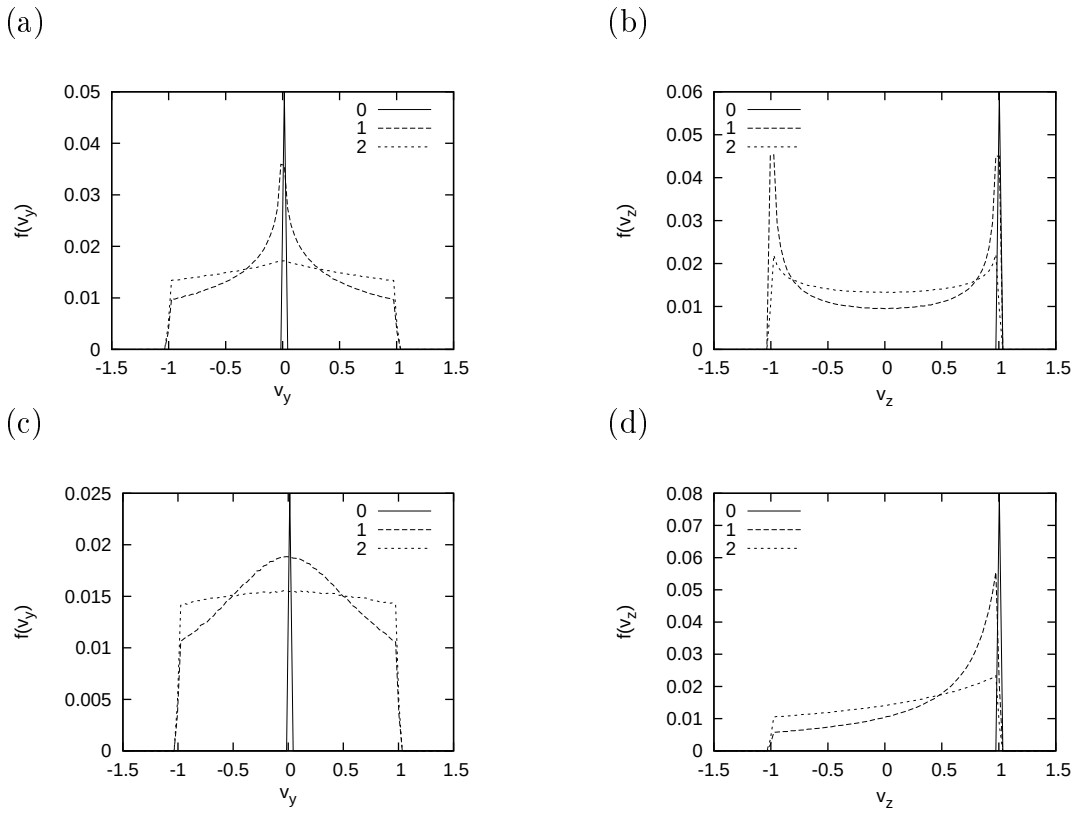

Figure 3.5: The electron distributions after the indicated number of scattering events. The collision cross sections used are the (a, b) isotropic 3.23 and (c, d) screened Coulomb cross sections.

gives the following distributions [19],

$$\begin{aligned} f(v_z) &= \frac{\varepsilon}{4\pi \ln(1+\varepsilon)} \int_0^{2\pi} d\phi \int_0^{\infty} dv_\rho v_\rho \frac{\delta\left(\sqrt{v_\rho^2 + v_z^2} - 1\right)}{1 + \frac{\varepsilon}{2}(1 - v_z)} \\ &= \frac{\varepsilon}{2\ln(1+\varepsilon)} \left[\frac{v_\rho}{1 + \frac{\varepsilon}{2}(1 - v_z)} \frac{\sqrt{v_\rho^2 + v_z^2}}{v_\rho} \right]_{v_\rho = \sqrt{1 - v_z^2}} \\ &= \frac{\varepsilon}{\ln(1+\varepsilon)\left[2 + \varepsilon(1 - v_z)\right]}, \end{aligned} \tag{3.35}$$

$$f(v_y) = \frac{1}{\ln(1+\varepsilon)\left[\frac{4}{\varepsilon^2}(1+\varepsilon) + v_y^2\right]^{1/2}}. \tag{3.36}$$

These functions are also successfully reproduced by the scattering test, as seen in Fig. 3.5c and 3.5d.

3.4.2 Collision Frequency

The Monte Carlo collisions are performed on a random selection of particles at each time step. With a constant collision frequency ν, the probability for a single particle to collide in the interval $[t,\, t + \Delta t]$ is $P_{collide} = 1 - e^{-\nu \Delta t}$, as modelled by a Poisson process. A simple approach would be to then perform a collision on each individual particle during a time step if a random value $R_3 \in [0,\, 1)$ is less than the probability of colliding $R_3 < P_{collide}$. For a large number of particles N_{part}, an equally large number of random values must be generated, which is quite slow. Rather than this method, a subset of $N_{collide} = N_{part} P_{collide}$ particles is randomly selected from the entire set and collisions are performed on all of them. While this method is much faster, it suffers the flaw of permitting a particle to collide only once in the step interval.

The probability that is calculated is actually the probability that a particle will collide *at least once* during the step. Due to the finite time step, there is a systematic error incurred due to the possibility of ignoring a single particle colliding multiple times. This probability can be calculated by subtracting the probability of a single collision, so that $P_{multiple} = 1 - e^{-\nu \Delta t} - \nu \Delta t e^{-\nu \Delta t}$. Then, the fraction of instances in which collisions are ignored is:

$$\frac{P_{multiple}}{P_{collide}} = 1 + \frac{\nu \Delta t}{1 - e^{\nu \Delta t}} \simeq \frac{\nu \Delta t}{2}. \tag{3.37}$$

The average number of collisions that are ignored per particle per step is

$$\langle N_{skip} \rangle = \sum_{n=2}^{\infty} (n-1) \frac{e^{-\nu \Delta t} (\nu \Delta t)^n}{n!} = e^{-\nu \Delta t} + \nu \Delta t - 1 \simeq \frac{(\nu \Delta t)^2}{2}, \tag{3.38}$$

with the fraction of the total being:

$$\frac{\langle N_{skip} \rangle}{P_{collide}} = \frac{e^{-\nu \Delta t} + \nu \Delta t - 1}{1 - e^{-\nu \Delta t}} \simeq \frac{\nu \Delta t}{2}. \tag{3.39}$$

In Fig. 3.6a, it is apparent the loss fraction is accurate, except when numerical fluctuations are greater than $\nu \Delta t$. It is important to keep the time step or collision frequency small so as to make the fraction of lost collisions ignorable. However, this should not affect isotropic scattering, since multiple collisions at the same time give the same result as a single collision.

A further difficulty arises in the case of the energy-dependent scattering distribution: that the collision frequency depends on particle velocity and position, $\nu = n(\mathbf{x})\sigma(v)v$. No longer can a global value be used for $P_{collide}$ to extract a selection of colliding particles, but it is still undesirable to check whether $R_3 < P_{collide}$ for every single particle. Therefore, the appropriate technique is a hybrid of the two methods, called the null collision method. First, as many particles as possible are eliminated by using the maximum possible fraction of colliding particles

$$\nu_{max} = max[n(\mathbf{x})\sigma(v)v] = max[n(\mathbf{x})]max[\sigma(v)v], \tag{3.40}$$

$$P_{max} = 1 - e^{-\nu_{max} \Delta t}. \tag{3.41}$$

Then from that group, the slower method of generating a random value for each particle and comparing with its actual collision frequency must be resorted to

$$R_3 < \frac{P_{collide}}{P_{max}} = \frac{1 - e^{-n(\mathbf{x})\sigma(v)v\Delta t}}{1 - e^{-\nu_{max} \Delta t}}. \tag{3.42}$$

If this condition is not true, then no collision is "performed", hence the null collision terminology. When the collision frequency does not vary significantly, this method is nearly as efficient as in the isotropic case.

Ohm's law provides a good test of the collision frequency and is a useful intermediate build step between the completely static cross-section test and the fully self-consistent plasma simulation. In this test, the plasma is completely homogeneous, and either a DC or an AC electric field is created in the y-direction. For

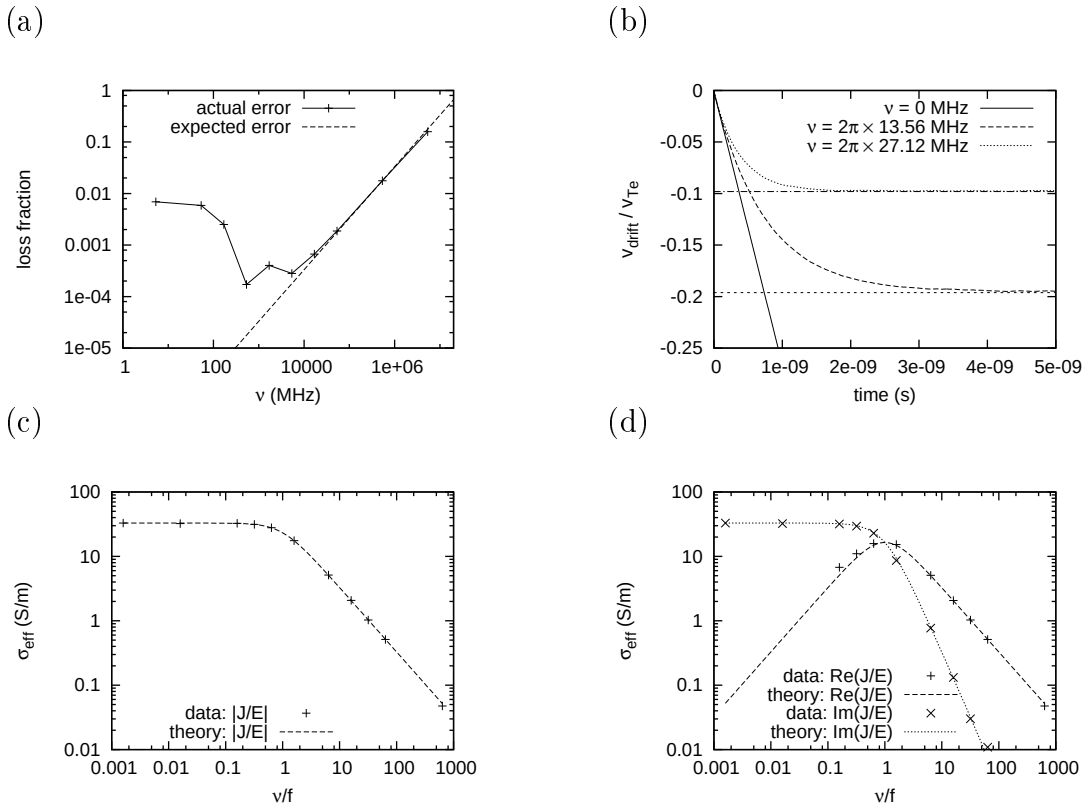

Figure 3.6: (a) Fraction that the actual number of collisions falls short of the expected number of collisions, as well as the expected loss fraction at high collisionality due to ignoring multiple collisions in a single time step. (b) Ohm's Law Test 1: Average drift velocity for electrons in a DC electric field with and without collisions. Parameters are $E = 2000$ V/m and $n_e = 10^{17}\,\mathrm{m}^{-3}$. (c, d) Ohm's Law Test 2: Conductivity in plasma driven by an AC electric field of frequency $f = 13.56$ MHz, amplitude $E = 2000$ V/m, and density $n_e = 10^{17}\,\mathrm{m}^{-3}$.

simplicity, the plasma is unshielded, so each particle feels the same field at the same time.

The electron equation of motion in a DC electric field is:

$$m\frac{dv}{dt} = -eE - m\nu v. \tag{3.43}$$

The steady-state solution provides the drift velocity as:

$$v_{drift} = \frac{-eE}{m_e\nu}. \tag{3.44}$$

This result is tested for a field of $E = 2000$ V/m and temperature of $T_e = 5$ eV in Fig. 3.6b, with the results shown normalized against the initial thermal velocity. There are no perceptible deviations from theory.

For an AC field, the plasma conductivity is the expected coefficient relating the electric field to the current,

$$\sigma_{eff} = \frac{J}{E} = \frac{n_e e^2}{m_e(\nu + i\omega)}. \tag{3.45}$$

Fig. 3.6c shows the magnitude of the conductivity, while Fig. 3.6d shows the real and imaginary components. The data points are absent for low collision frequencies because the real part becomes negligible relative to the imaginary part and easily susceptible to noise. Otherwise, the results match closely with theory. Since both the scattering distribution and collision frequency are successfully verified by the controlled tests, it is reasonable to enable collisions in conjunction with self-consistent dynamics.

3.5 Parallel Computation

As the amplitude of the driving wave is decreased, the signal to noise ratio increases. This is combated by adding more particles to the simulation, which increases the number of calculations required per step. Therefore, the simulation program was parallelized so that the work could be divided among multiple CPUs. This was accomplished in software using MPI commands and the hardware was provided by Westgrid.

The proceeding describes the task of parallelizing a PIC simulation conceptually, with a schematic found in Fig. 3.7. The particles are initialized by all processes

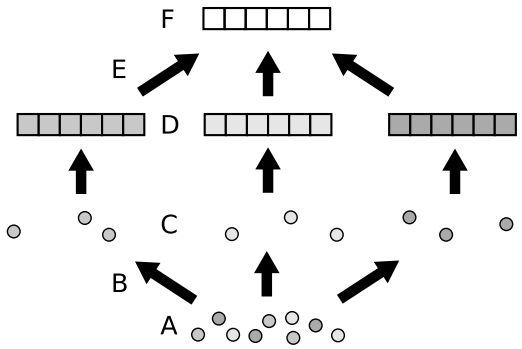

Figure 3.7: Representation of the work allocation among multiple processors. The plasma particles and their resultant fields are divided among all CPUs (represented by different shades), but the fields are superposed at each time step before the particle motion is updated. A description of each step is found in Section 3.5.

in unison (A), but randomly distributed to each task before any time progression (B). Each task independently tracks the motion of its own group (C), and calculates the mesh properties (density, temperature, current, etc.) of only those particles (D). Since the fields on the mesh can be superposed, they are summed over all tasks (E) and the answer is broadcast back to each CPU (F). After the electric fields have been found using the collected mesh values, each task interpolates the values back to its group of particles and adjusts their motion accordingly. This routine occurs between Steps (2) and (3) from Fig. 3.2 during every step.

Once each CPU has the complete set of particle moments, they all perform the same calculation of the new fields. This redundant behaviour is justified by noting that the number of grid points is much smaller than the number of particles, even for a single CPU, so only a small amount of the total work is repeated. The proper method would be to partition the mesh out among the processes as well. This would be quite difficult, however, because some properties, notably the temperature, are spatially smoothed, requiring additional communication among tasks about the values at the division edge. The gained efficiency would not offset the complexity of the necessary changes to the program.

3.5.1 Program Scalability

If the program runs on multiple processors, a speed-up in computation time will be gained. The speed-up is a simple quantity to determine by running the program with different numbers of CPUs and tabulating the results as $T(1)/T(p)$, where $T(p)$ is the time taken for p processes to complete the simulation. One can see in Table 3.1

# of particles	250,000	1,000,000	4,000,000
serial run time	2608 s	10367 s	41474 s
2 processes	1.96	1.94	1.98
3 processes	2.58	2.95	2.94
4 processes	3.23	3.95	3.90

Table 3.1: The serial run time and some speed-up rates for a program running with nonlinear dynamics on a 100 cell mesh. A speed-up of 2 indicates the program completed twice as fast as a serial run.

that the speed-up is generally greater when there are more particles involved. This is because particle manipulation does not involve interprocess communication, so a larger percentage of time is spent actually advancing the system.

Unfortunately, it is also apparent that the speed does not increase linearly as processes are added. One would expect that more processes would decrease proportionately the time required to execute a program, but there is also more communication overhead, usually proportional to $\log p$, where p is the number of processes. Therefore, a more frequently used measure of parallel performance is the efficiency, the total CPU time required for p parallel processes to complete a run relative to that of a serial calculation,

$$E = \frac{T(1)}{pT(p)}. \tag{3.46}$$

The efficiency will fall when any process is waiting for others to reach a checkpoint, or when all the processes are synchronizing data, which does not contribute to the actual progress of the calculations.

The disadvantages of looking at only the efficiency is that the reason for decreasing efficiency is not quickly apparent. Therefore, Karp and Flatt [6] describe another metric that can identify the cause of lost efficiency, the serial fraction. If the time to run the program is

$$T(p) = T_s + \frac{T_p}{p}, \tag{3.47}$$

where T_s is the time taken for serial calculation and T_p the time that it runs perfectly parallel. By noting that $T(1) = T_s + T_p$ and defining the serial fraction as $SF = T_s/T(1)$, it can be written

$$SF = \frac{T(p)/T(1) - 1/p}{1 - 1/p}. \tag{3.48}$$

Unlike the efficiency, this parameter grows as CPU time is wasted; a small value

(a) (b)

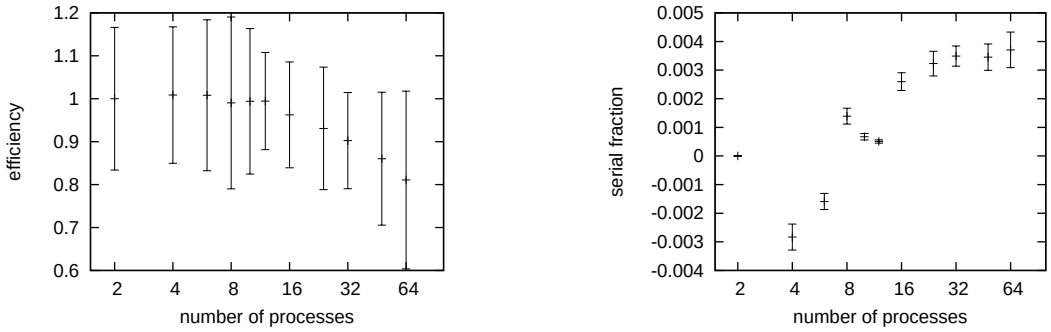

Figure 3.8: The (a) efficiency and (b) serial fraction parallel performance metrics for a nonlinear simulation with collisions performed on a 200-cell mesh with 2,000,000 particles. Each point represents the averaged result of 8 tests. The use of both cores of dual core processors was enforced during these tests, so there is no serial processing data point. The definition of the serial fraction is strictly positive, but the 2 process data were used in lieu of actual serial data.

indicates dominantly parallel operation in which the processes are working in lockstep with one another. If the processes are not assigned equal workloads and spend time waiting for each other to complete tasks before synchronizing, then they have a high load imbalance. The load balance is highly susceptible to changes in the number of processes, and therefore, will show up as abrupt changes in SF. On the other hand, communication overhead is highly predictable, proportional to $\log p$. In this particular case, there is also duplication of some mesh calculations, proportional to p. These predictable effects result in a smooth increase in the serial fraction.

Fig. 3.8 makes apparent that the efficiency drops secularly as the number of processes is increased, but not with the $\log p$ relationship predicted by theory. There is nearly perfect efficiency for all tests of 12 processes or fewer, and an apparent linear drop with 16 or more. This suggests that the duplication of mesh calculations is insignificant when there are greater than 800 particles per cell per process. Despite the high efficiency for few processes, the serial fraction clearly shows that load balancing is an issue. There are abrupt fluctuations for less than 12 processes. Once the number of processes has exceeded 16, load imbalances become less significant relative to the communication overhead, and the serial fraction exhibits a smooth growth.

The effect of particle number is presented in Fig. 3.9. Despite the greater run time necessary, the efficiency improves as more particles are added. Interprocess

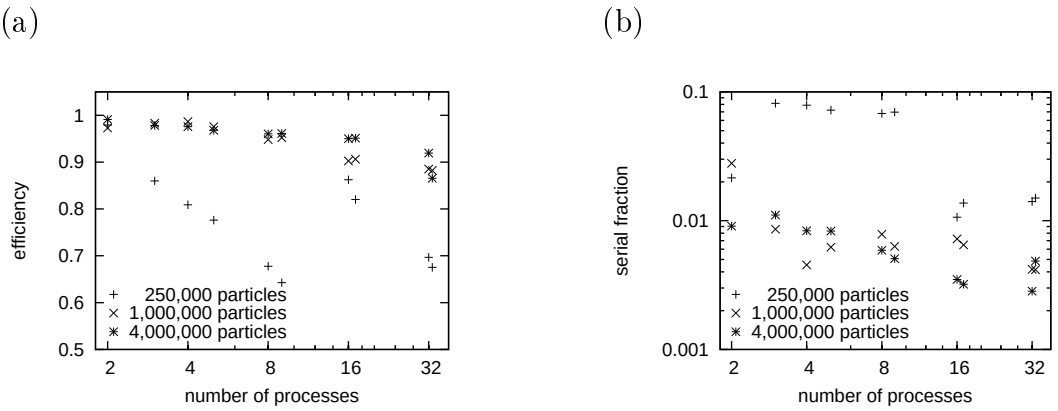

Figure 3.9: The (a) efficiency and (b) serial fraction parallel performance metrics for a nonlinear simulation performed on a 100-cell mesh with different numbers of particles. Each point represents a single trial.

communication only involves sharing mesh values, which remain fixed in this test. One can also see that the serial fraction becomes much smoother because a larger number of particles is more equally divided among processes. As the number of particles is increased, the load imbalances become less significant and the communication overhead becomes the rate limiting factor.

In general, when the number of particles N per process is large relative to the number of grid points M, the serial fraction is low and the efficiency is high. The tests show the number of processes must remain below the threshold $N/Mp > 800$. Most of the simulations are run with 200 cells and 2 million particles, and therefore, the number of processes used was either 4 or 8.

Chapter 4

Results

All the properties of the ICP that were analyzed related to the skin layer. These include the field amplitudes, the skin depth, the surface impedance, and the ponderomotive force. They are affected by a number of system parameters, of which the following were investigated: the amplitude E_{dr} and frequency f of the driving wave, the electron-neutral collision frequency ν, the ion mass m_i, and the temperature of the plasma T_e. When the ion temperature was applicable, it was always set to $T_i = 0.1T_e$, since low pressure discharges do not have thermal equilibrium between species [10]. The plasma length was occasionally varied, but this was only done to match results of other papers, and all main results use a length of 10 cm.

A majority of the results are run in three of the four possible modes: linear, nonlinear collisionless, and nonlinear collisional. In linear mode, the particles are not influenced by either the magnetic or longitudinal electric fields. The fields are still calculated so that the ponderomotive force can be recorded, but it has no effect on the particles. Nonlinear collisionless mode mimics proper physical behaviour with regard to particle-field interactions, but there are no direct collisions. The nonlinear collisional mode adds electron-neutral collisions to the simulation at a rate of $\nu = 2\pi$ MHz. Linear collisional mode was used to test collisions, but ignored when scanning amplitude-frequency space, because of the inaccuracies inherent in the simulation during high collision rates (Sec. 3.4.2).

4.1 Skin Fields

4.1.1 Electric and Magnetic Field Amplitudes

While most theories describe quantities in terms of E_0 or B_0, the electric and magnetic fields immediately inside the surface of the plasma, the independent variable for many of the tests is the amplitude of the driving electric field E_{dr}. This is because E_{dr} is a directly controllable parameter of the simulation and is easier to plot

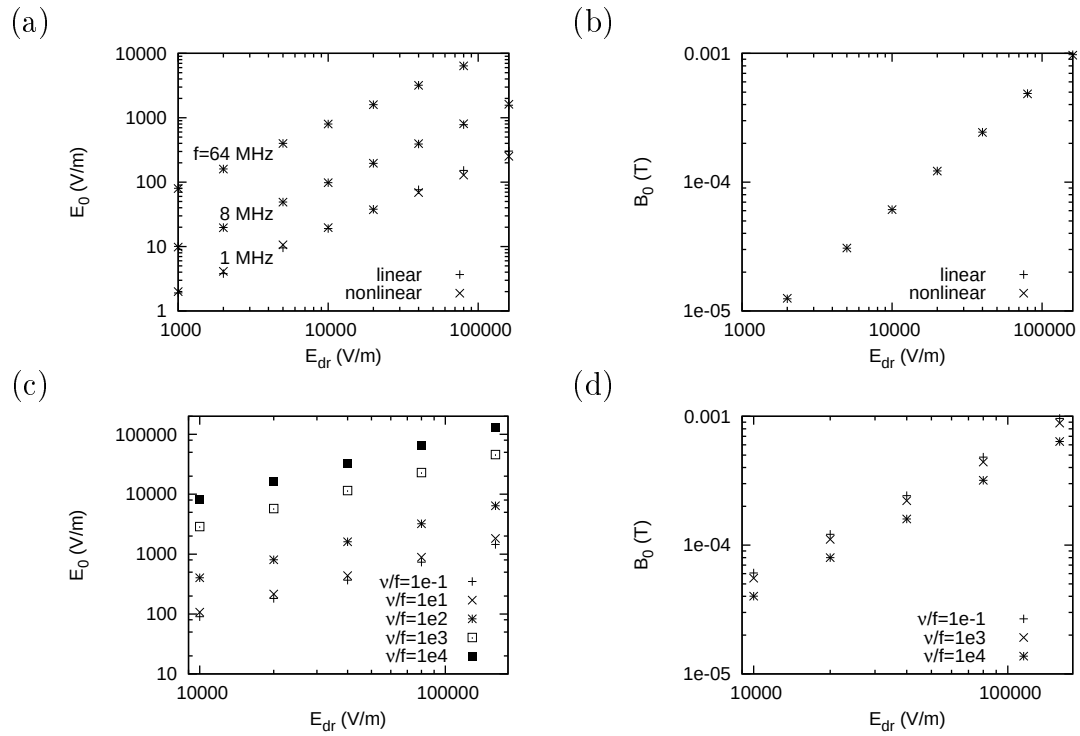

Figure 4.1: The field amplitudes 2 mm inside the plasma. (a) The electric field for three frequencies and (b) the magnetic field for all frequencies in linear and nonlinear collisionless mode. Plasma parameters are $L_{pl} = 10$ cm, $n_e = 10^{17}\,\mathrm{m}^{-3}$, $T_e = 10$ eV. (c) The electric field and (d) magnetic field at a frequency of $f = 13.56$ MHz for different collision rates. Plasma parameters are $L_{pl} = 4$ cm, $n_e = 10^{17}\,\mathrm{m}^{-3}$, $T_e = 5$ eV.

on a grid. Unfortunately, it is not physically observable because the reflected wave from the plasma partially cancels the incoming wave. As can be seen in Fig. 4.1, the amplitudes of all these fields are nearly proportional to one another, with the electric field in the skin layer also related to the driving frequency

$$E_{dr} \propto B_0 \propto E_0/f. \tag{4.1}$$

The effect of temperature and the nonlinear fields appears to be very small, but growing collision rates cause an appreciable increase of the electric field and a small decrease of the magnetic field inside the plasma. Note that nearly all time dependent plasma parameters, such as the terms E_0 and B_0, are measured 2 mm inside the plasma because the simulated fields must be sampled at a finite number of steps from the boundary.

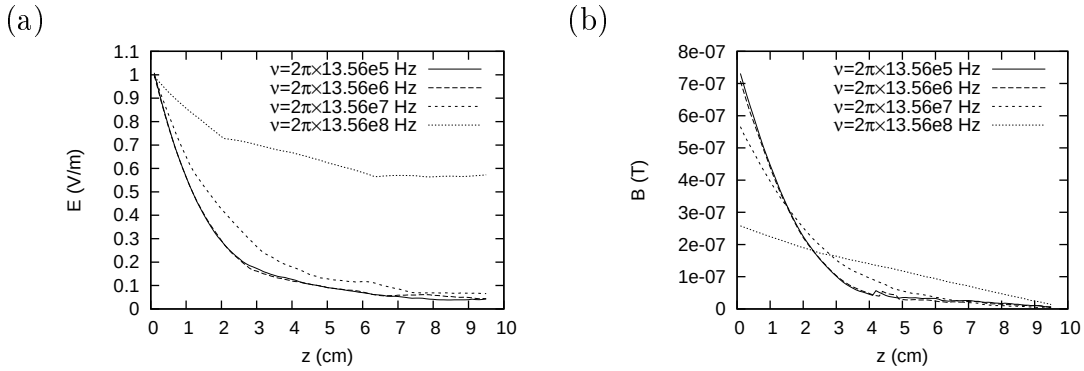

Figure 4.2: The field amplitude envelopes in the skin layer during a linear simulation with a driving frequency $f = 13.56$ MHz, plasma length $L_{pl} = 10$ cm, density $n_e = 10^{17}\,\mathrm{m}^{-3}$, and temperature $T_e = 5$ eV. All amplitudes are normalized to E_0, the electric field at the surface.

4.1.2 Electric and Magnetic Field Profiles

The profile of the electric and magnetic fields in the skin layer were tested with linear dynamics (Fig. 4.2). When comparing the results qualitatively with the linear theories in Fig. 2.3, it appears that at moderate collision frequencies, the electric field matches the local approximation (Fig. 2.3a). At high collision rates, however, the skin depth is much greater than the simulated device length of 10 cm, which makes comparison difficult with linear theories where it was assumed that the electric field goes to zero at the right boundary. Meanwhile, the form of the magnetic profile seems also to match the local approximation, but the amplitudes do not show the same relationship with collision rates as that in Fig. 2.3b.

4.2 Mobile Ions and Ion Mass

Ordinarily, a DC sheath exists at the edge of the plasma, because electrons are more mobile than ions and more rapidly lost to the walls [10]. Electron loss does not occur in this PIC simulation because the particle number is held constant and so all particles reflect spectrally when they reach a wall. Still, a voltage drop does develop in the skin layer because the PMF is mass independent, and therefore, the mobile electrons are more easily accelerated away from the boundary. Therefore, the density of the ions at the boundary should depend on their mobility and the period of time they have had to move.

A number of tests were performed to check the effect of singly-charged ions of different masses on the simulated plasma. The ion mass was varied over three values,

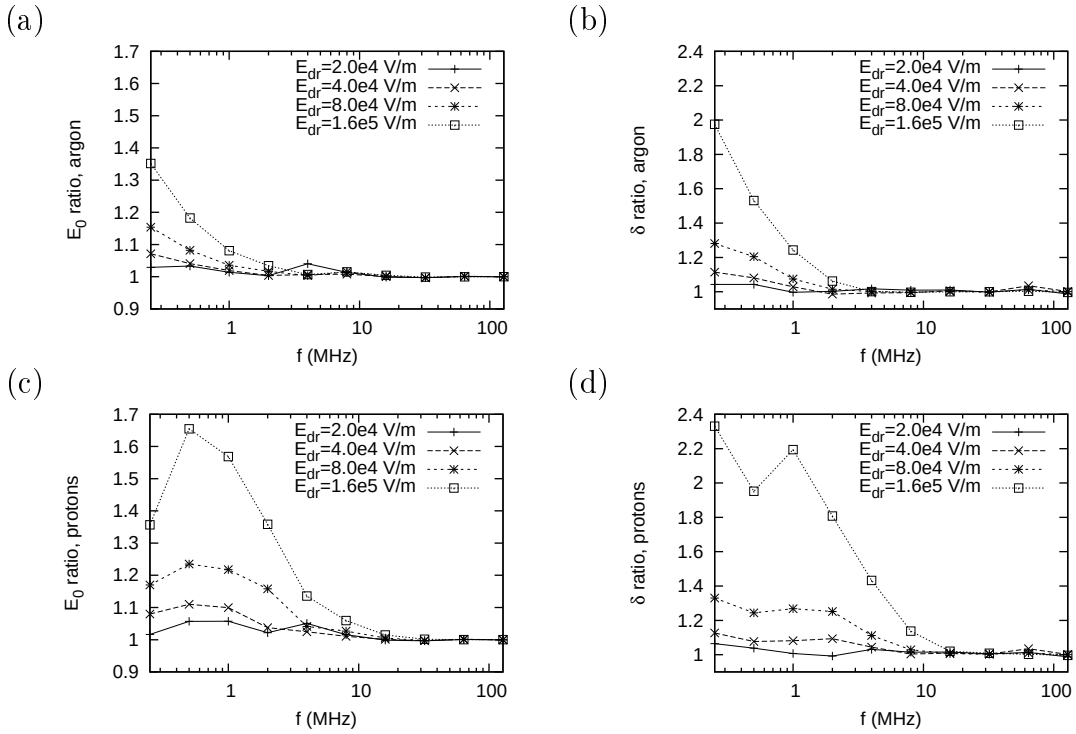

Figure 4.3: The effect of an ion mass relative to immobile ions as evidenced by (a, c) the electric field amplitude E_0 and (b, d) the skin depth δ for (a, b) heavy singly-charged argon ions and (c, d) protons in a plasma with length $L_{pl} = 10$ cm, density $n_e = 10^{17}\,\mathrm{m}^{-3}$, electron temperature $T_e = 10$ eV, and ion temperature $T_i = 1$ eV.

$1837m_e$ for protons, $74400m_e$ for singly-charged positive argon ions, and immobile ions simulated as a uniform neutralizing background. For most values of the driving wave parameters, the effect of ion mass on the plasma was minimal. However, for the lowest frequencies and highest field amplitudes tested with mobile ions, the skin depth and internal fields were increased by as much as a factor of 2 from the immobile ion case, as seen in Fig. 4.3.

The mobile ions appear significant in only a small fraction of the investigated regime, while they require a doubling in computation time to accommodate the additional particles. Therefore, to improve speed they should be removed for the remainder of testing and replaced by a uniform neutralizing background. However, the validity of Fig. 4.3 must be sufficiently proved before the ions can be ignored. The simulations usually run for 2 periods, but the ions spend some of that time reaching equilibrium. Since the plasma properties are averaged over the full two periods, the ion effects may be under-reported.

The distribution of ions in the skin layer strongly affects the longitudinal electro-

static force on the electrons. Therefore, it is important to take data after equilibrium in the skin layer has been reached. Since the ion temperature is set to $T_i = 0.1T_e$, the thermal motion of the ions is very small and movement is primarily due to the ponderomotive force. The time required to reach equilibrium is estimated as the time it takes an initially stationary ion to transverse the skin layer under the influence of the PMF, given by

$$t_{transit} = \sqrt{\frac{m_i \delta}{eF_p}} < \frac{1}{f}. \tag{4.2}$$

When the ion transit time is greater than the wave period, a majority of the simulation time is performed away from equilibrium, and therefore, the results are not fully accurate.

Fortunately, this condition only fails in the same small regime that already exhibits a mobile ion effect. Therefore, it is deemed reasonable to eliminate the ions in favour of a uniform neutralizing background. However, to amend this simplification properly, the ions must be made mobile, simulations run for a longer period of time, and averaging started after equilibrium has been reached.

4.3 Skin Depth

Since skin-layer profiles can be noisy, it is difficult to measure the skin depth using the derivative at the surface. Instead, the actual point at which the field drops to $1/e$ of its initial value is calculated. This is also done for some intermediate points as well, the results of which are averaged together to get a more reliable estimate.

This method is applied to the maximum envelope of only the magnetic field profile because it is much less prone to noise than the electric field. The noise exists because $F^+ \sim -F^-$, so that the magnetic field is large $B \propto F^+ - F^- \sim 2F^+$, but the electric field is near to zero $E \propto F^+ + F^- \sim 0$. To acquire the envelope, a snapshot of $B(z)$ is taken 40 times per period. These snapshots are then scanned to produce two profiles. The first is the time independent profile, made up of the maximum value of all the profiles point by point, regardless of which snapshot each value comes from. The second is the maximum area profile, the single time profile enclosing the greatest integrated area. These two profiles are then averaged together to give the maximum envelope.

The purpose of this technique is to smooth the results, but may reinforce the values at the surface and reduce those inside the plasma. Any underestimation of the skin depth due to this technique can only be tested with the currently available tools

by an extremely high definition simulation. The results (Fig. 4.4) are surprisingly smooth considering the empirically developed data extraction method.

One can see that tests in linear mode (Fig. 4.4a, b) give a skin depth independent of the driving wave amplitude. The skin depth is constant in the local regime, but decreases as the frequency is increased in the anomalous skin effect regime, and matches the theory in both cases. At very low frequency, the skin depth reaches a maximum because of constraints of the numerical simulation, such as finite plasma length. The transition between the local and anomalous skin effect regimes can be seen to be at about $f = 30$ MHz, of the same order as the theoretical transition at $f = v_T/\sqrt{\pi}\delta_a = 81$ MHz. Within the local regime, the skin depth is level at $\delta = 1.7$ cm, the theoretical local value.

The behaviour is quite different in nonlinear collisionless mode (Fig. 4.4c, d). As the amplitude of the driving wave is increased, the frequency range of the anomalous skin regime becomes smaller and smaller until it is eventually no longer present above $E_{dr} = 3 \times 10^6$ V/m. At frequencies below the anomalous skin regime, the skin depth is independent of the frequency, and becomes related to the magnetic field by roughly a power of five,

$$\delta_{nl} \propto f^{0\pm0.03} B_0^{-0.19\pm0.03}. \tag{4.3}$$

It is appropriate to call this area the nonlinear regime, as it exhibits behaviour very close to the $f^0 B_0^{-1/5}$ relationship predicted by the nonlinear theory. The boundary between the anomalous and nonlocal regimes is approximately given by the line $E_{dr} = 9 \times 10^{-10} f^{2.0\pm0.1}$. These dependencies are acquired from data ranging from $f = 0.25$ to 128 MHz and $B_0 = 7 \times 10^{-6}$ to 8×10^{-3} T.

As can be seen in Fig. 4.1d, collisions reduce the magnetic field. This has the effect of damping the nonlinear effects and increasing the skin depth (Fig. 4.4e, f) towards its linear value. There still exists a small diagonal band where the nonlinearities appear to remain dominant, but at high amplitudes, collisions interfere with the cyclotron gyration and thermal effects are once again dominant.

4.4 Surface Impedance

The surface impedance is calculated in two different ways: directly by using the electric and magnetic fields in the skin layer, and indirectly via the power absorption. Since the first method involves determining the phase shift between the fields, it is slightly less precise than the second method. However, both can reasonably be used interchangeably.

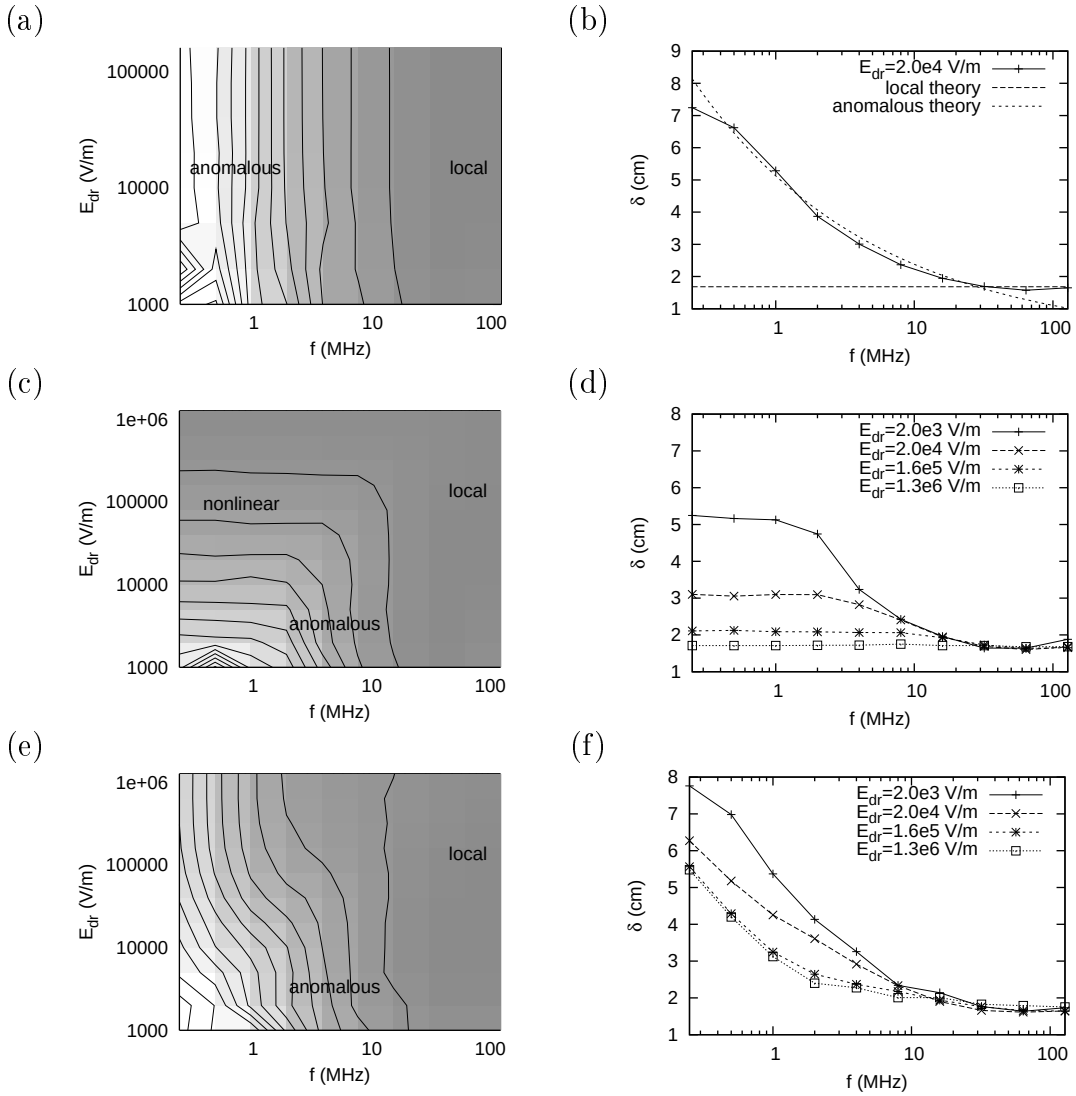

Figure 4.4: The skin depth as calculated with the magnetic field profile in a plasma with length $L_{pl} = 10$ cm, density $n_e = 10^{17}\,\mathrm{m}^{-3}$, and temperature $T_e = 10$ eV as a function of driving amplitude and frequency in (a, b) linear mode, (c, d) nonlinear collisionless mode, and (e, f) nonlinear collisional mode with collision frequency $\nu = 2\pi$ MHz. Contour plots show lines of equal skin depth. Results at low amplitude are less reliable than those high amplitude.

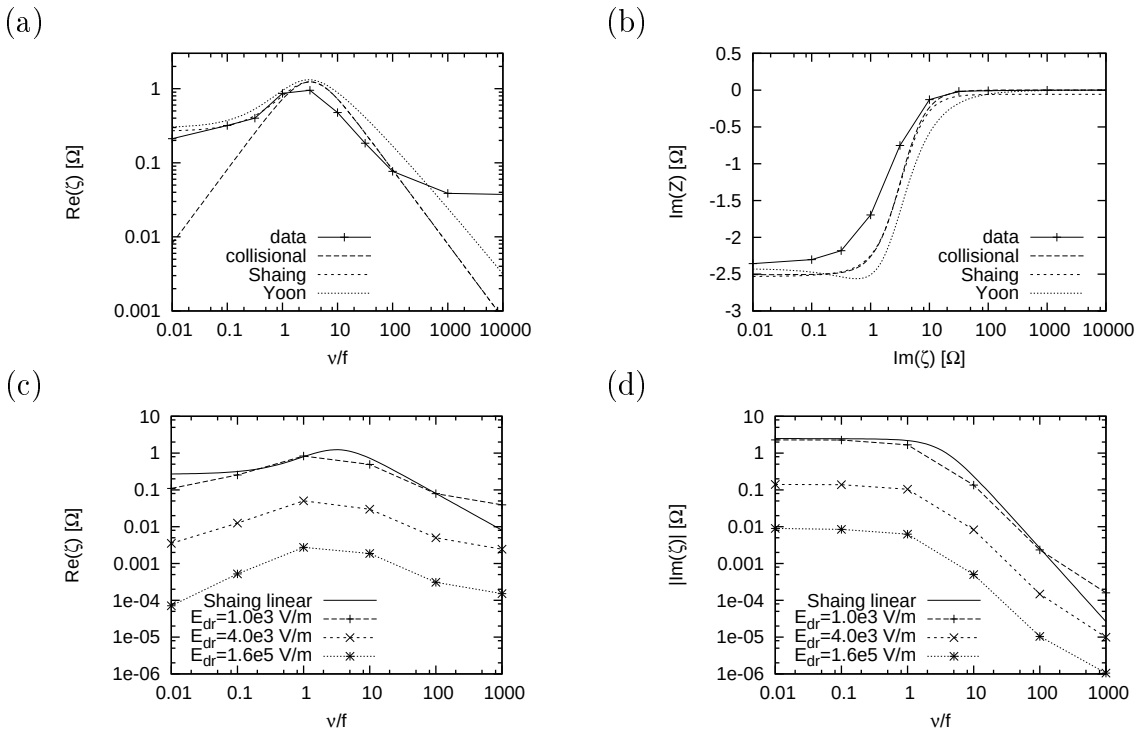

Figure 4.5: The (a) real and (b) imaginary components of the surface impedance from a simulation in linear mode compared with the Shaing and Yoon formulas and the local approximation. The (c) real and (d) imaginary components of the surface impedance in nonlinear mode, also compared with the Shaing formula. The plasma parameters in both cases are length $L_{pl} = 4$ cm, density $n_e = 10^{17}\,\mathrm{m}^{-3}$, and temperature $T_e = 5$ eV.

A simulation is performed with linear dynamics at a single driving frequency $f = 13.56$ MHz over a number of collision rates (Fig. 4.5a, b) and it is found to match the theoretical curves from Shaing *et al.* [16] and Yoon *et al.* [25] very well (Fig. 2.3). The only deviation occurs in the real component at high collision frequency, due to the fact that the collision model becomes increasingly inaccurate and the exponentially decreasing impedance is more susceptible to statistical fluctuations.

Attempting the same test with nonlinear dynamics shows that the relationship to the collision rate remains the same as the linear case at all driving wave amplitudes. However, as the amplitude is increased, the impedance drops proportionately. This suggests that the total power absorbed by the plasma is proportional to the amplitude, an intuitive result.

In linear mode, the power absorption is independent of the amplitude of the driving electric field and grows with frequency as $f^{2/3}$ in the anomalous region, as expected (Fig. 4.6a, b). Linear theories suggest that the plasma is completely

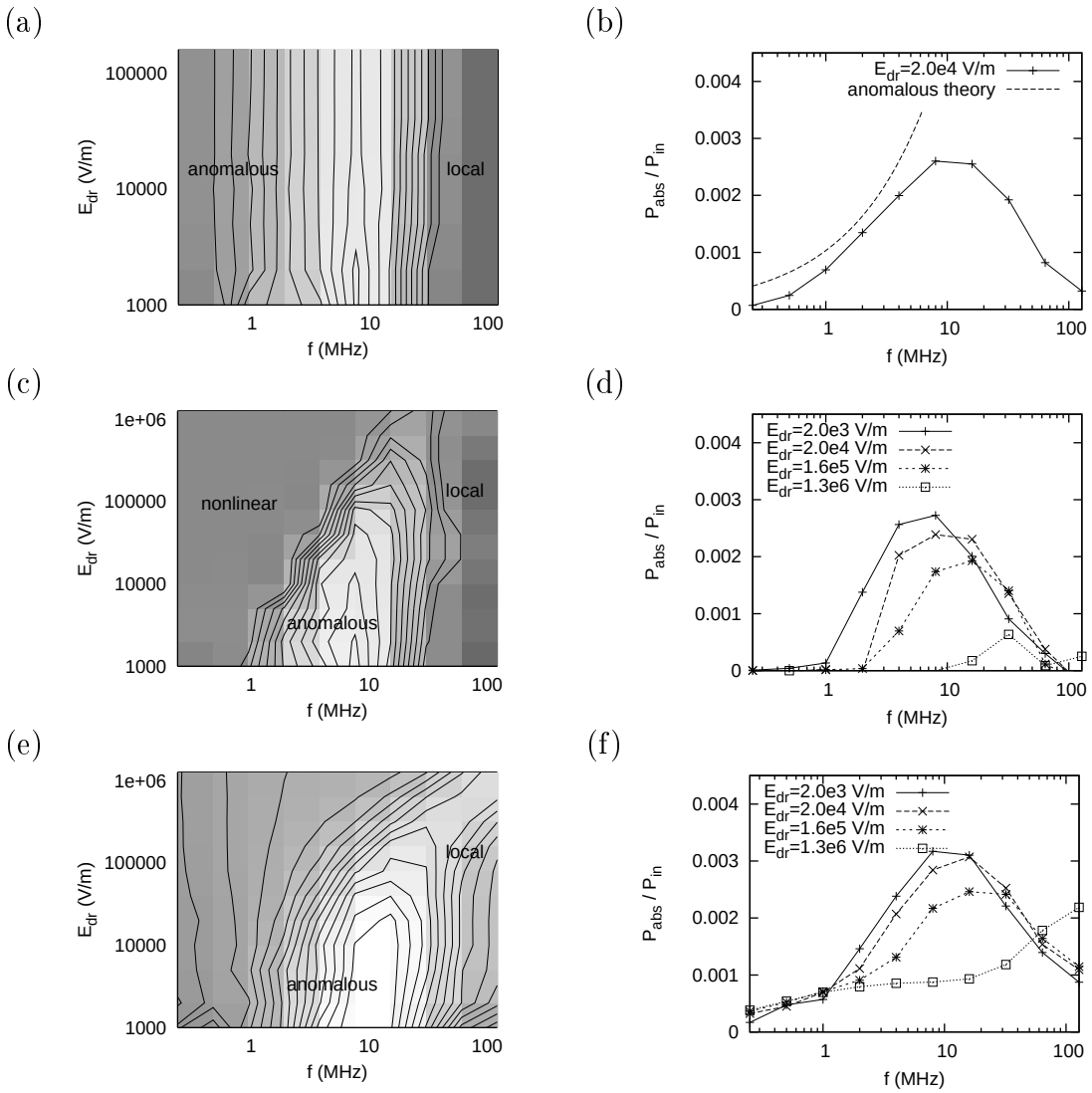

Figure 4.6: The fraction of power absorbed by a plasma with length $L_{pl} = 10$ cm, density $n_e = 10^{17}\,\mathrm{m}^{-3}$, and temperature $T_e = 10$ eV as a function of driving amplitude and frequency in (a, b) linear mode, (c, d) nonlinear collisionless mode, and (e, f) nonlinear collisional mode with collision frequency $\nu = 2\pi$ MHz. Contour plots show lines of equal absorption ratio. Results at low amplitudes are less reliable than those high amplitudes.

reflective at high frequency, but since the predicted absorption at the boundary between the two regimes is not continuous, there is an observed transition zone between the local and anomalous skin effect regimes that occurs between about 5 MHz and 150 MHz. Absorption peaks in this transition, but is close to zero otherwise (Fig. 4.6a, b). The reason for high reflectivity at both high and low driving frequencies is described elsewhere [22].

When switching to nonlinear mode, half the region that was absorptive in the linear case becomes reflective (Fig. 4.6c, d). The nonlinear regime that was seen in the skin depth plots is present as a region in which little power is absorbed by the plasma. As the amplitude of the driving wave is increased, the absorption is reduced, as is the range of frequencies under which it takes place. This has the effect of increasing the frequency of peak absorption. It is apparent that energy absorption in the anomalous skin regime is much higher than in other regimes; the EM wave is almost completely reflected at both high and low frequencies and high amplitudes.

Adding collisions to the simulation causes the expected result of increasing the overall absorption rate, especially at high amplitude and frequency (Fig. 4.6e, f). This is more obvious under conditions that previously were totally reflective, as the anomalous skin effect regime appears rather unchanged. The reason for greater absorption in the high-frequency/high-amplitude region is likely because electrons quivering in response to the AC field contain a lot of energy which usually time-averages to zero, but with collisions becomes the main source of energy for the plasma.

4.5 Ponderomotive Force

The ponderomotive force is calculated directly by multiplying the electric current and magnetic field inside the skin layer and taking the average over a wave cycle. Since the first approximation of the PMF is proportional to the electric field squared and inversely proportional to the frequency squared, it is difficult to see smaller effects in a direct plot. A simple solution is to show the ratio between the actual value and the cold-plasma approximation.

When using linear dynamics, the PMF profile in the skin layer (Fig. 4.7a) is most similar, at least in amplitude, to the theory of Smolyakov *et al.* [17] (Fig. 2.6c). The amplitude is related to the square of the transverse electric field, as expected (Fig. 4.7b). The cold-plasma approximation also suggests that the amplitude is inversely proportional to the square of the driving frequency. However, this is not so in a

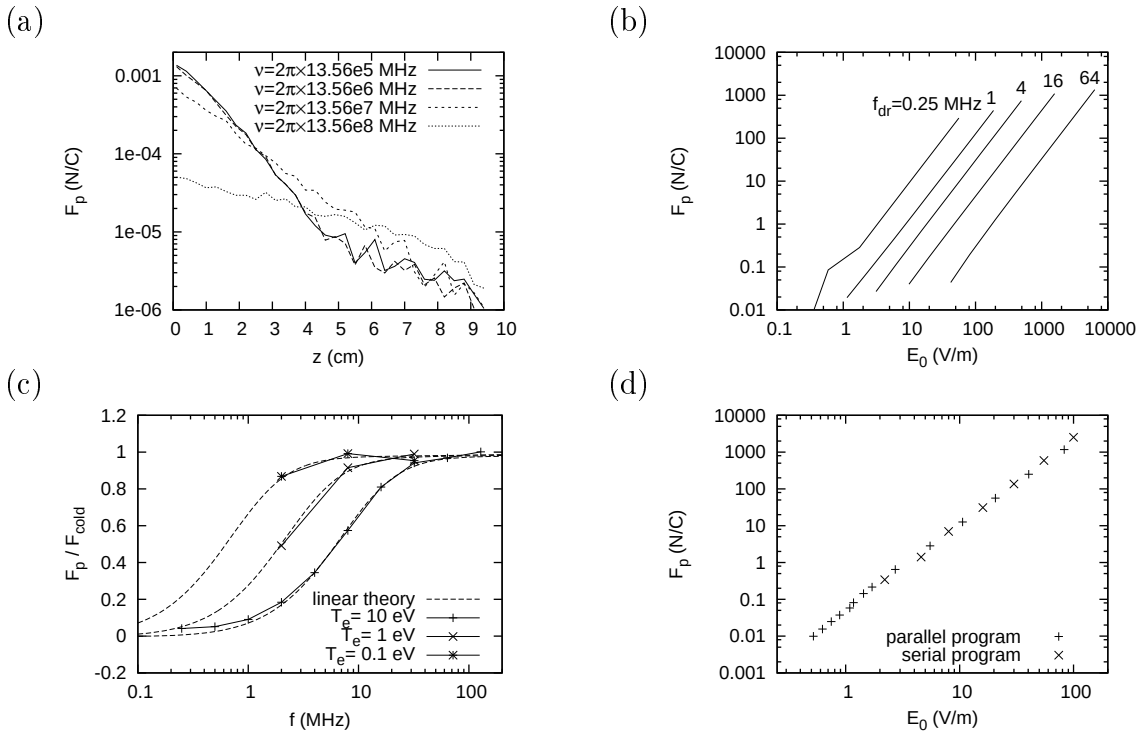

Figure 4.7: (a) The PMF profile in the skin layer during a linear simulation with a driving frequency $f = 13.56$ MHz, plasma length $L_{pl} = 10$ cm, density $n_e = 10^{17}\,\mathrm{m}^{-3}$, and temperature $T_e = 5$ eV. Amplitudes are normalized to E_0, the electric field at the surface. (b) The PMF in linear mode at $T_e = 10$ eV is proportional to the square of the electric field at all frequencies. Each line shows an individual frequency. (c) The ratio of the PMF in linear mode at $T_e = 10$ eV to the cold-plasma approximation compared to Smolyakov *et al.* [17] (Eq. 2.55) with a skin depth of $\delta = 2$ cm. (d) The PMF in nonlinear mode at frequency $f = 0.5$ MHz and $T_e = 10$ eV, which fits well to $F_p \propto E_0^{2.3}$ and provides evidence that the parallelized simulation program gives the same results as the original serial program.

thermal plasma, as evidenced by the fact that the spaces between the frequency lines are not identical.

When dividing out the dependence on electric field and frequency, Fig. 4.7b is recast as the 10 eV curve in Fig. 4.7c. The Smolyakov theory [17] corroborates the results at different temperatures extremely well. From this plot, it is more easily seen that thermal motion causes the PMF to become dependent on the frequency in a more complex way than that predicted by the cold-plasma approximation. The cold-plasma approximation applies at high frequencies because the particles quiver in response to the fields and forces time-average to zero. But at low frequency, there is a reduction in the PMF because the hot particles pass through the skin layer quickly and are influenced by the fields only briefly. High-speed particles make a greater contribution to the current than low-speed ones, so the current and PMF become reduced. The transition frequency is proportional to temperature because at lower temperatures, there are a larger fraction of cold particles to maintain the PMF.

In nonlinear mode, the PMF appears to retain a power relationship with the electric field, but the exponent is not the cold-plasma value of 2. This was known from data acquired with the original serial PIC simulation (Fig. 4.7d), which correspond to an exponent of 2.3. However, it was believed that at low driving amplitudes, the relationship would return to the cold-plasma approximation, regardless of temperature. With the parallel program, the regime of very low driving amplitude ($<$1 V/m) became accessible, but from the new data, it still appears that there is no change in the PMF at high or low amplitudes. However, further evidence will be presented that indicates this is simply because the samples are still well inside the nonlinear regime, as these data were calculated for a low frequency of $f = 0.5$ MHz, where the nonlinear regime covers a large range with a very low minimum amplitude.

In linear mode (Fig. 4.8a, b), the PMF is independent of amplitude. It is equal to the cold-plasma approximation at high frequency, but as the frequency drops, thermal motion causes the force to be reduced. This plot looks similar to the inverse of the linear skin depth results in Fig. 4.4b. For instance, the maximum PMF at high frequency occurs because the plasma is in the local regime, while the region of rapid change in PMF corresponds to the anomalous skin regime.

When using nonlinear mode (Fig. 4.8c, d), the PMF behaves as the skin depth does. It exhibits an anomalous skin regime when the amplitude of the driving wave is low and a nonlinear regime at large amplitudes and low frequencies. In the nonlinear regime, the PMF is almost independent of frequency, and as the amplitude increases, it becomes restored to its cold-plasma value. This new effect works to counteract

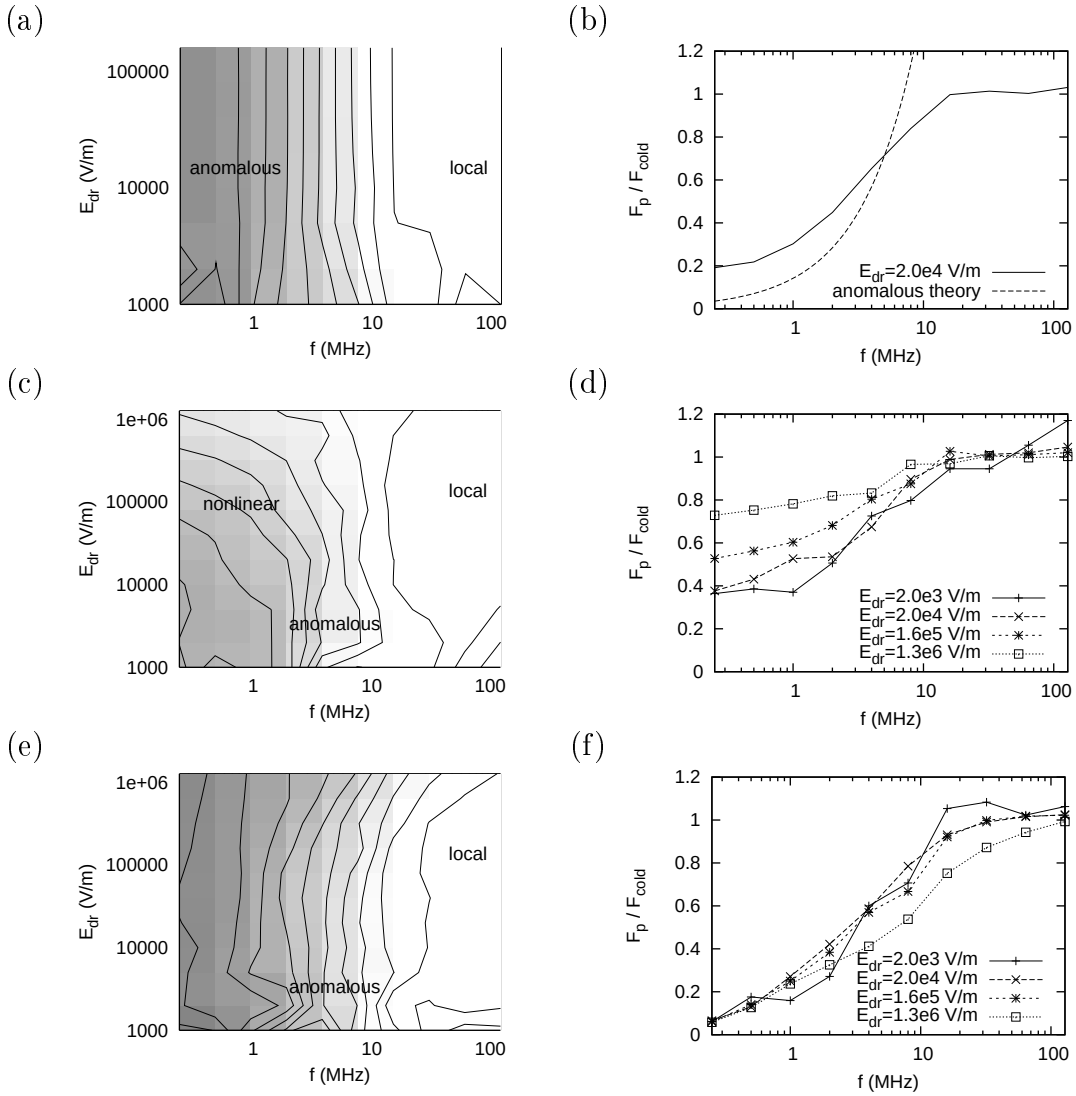

Figure 4.8: The ratio of the ponderomotive force to the cold approximation in a plasma with length $L_{pl} = 10$ cm, density $n_e = 10^{17}\,\mathrm{m}^{-3}$, and temperature $T_e = 10$ eV as a function of driving amplitude and frequency in (a, b) linear mode, (c, d) nonlinear collisionless mode, and (e, f) nonlinear collisional mode with collision frequency $\nu = 2\pi$ MHz. Contour plots show lines of equal skin depth. Results at low amplitude are less reliable than those high amplitude.

the suppression of the PMF at low frequency caused by thermal motion. Despite the skin depth dependence being removed from these plots of the PMF, the regime boundaries are still visible, albeit not as clearly as for the skin depth. This indicates the PMF is directly affected by the nonlinearities, and not entirely due to the change in skin depth.

Finally, when running in nonlinear collisional mode (Fig. 4.8e, f), it appears as if all nonlinear behaviour is cancelled and the PMF becomes nearly independent of amplitude again. This is a much stronger response than the skin layer exhibited, and reinforces the idea that the ponderomotive force is partially independent of the skin depth. The only difference noted between the linear and collisional cases is a small reduction in the force at high frequency and amplitude.

4.6 Regime Boundaries

Previously, the regimes were defined by behavioural differences in the plasma. A more quantitative approach is to fit the theoretical skin depth to the data to find how well and where they match. In Fig. 4.9, the plots on the left show the regions in amplitude-frequency space where the data deviate from each formula in Table 2.1 by 10% or less. The plots on the right show the actual values along some line through the space that is encompassed by each regime being tested.

Fig. 4.9a shows the results of a linear mode simulation, in which the space is divided between the anomalous skin effect regime at low frequency and the local regime at high frequency. Fig. 4.9b shows nonlinear collisionless mode, in which the anomalous skin effect regime now falls in between the local regime and a new nonlinear regime. Finally, Fig. 4.9c shows nonlinear collisional mode, in which the nonlinear regime has disappeared, except for the area where the nonlinear theory basically coincides with the anomalous theory.

Fig. 4.9d shows the line $f = 128$ MHz, which falls inside the local regime for all modes. The results from all modes coincide with theory very well, deviating only slightly at low amplitude, when statistical fluctuations in the fields can be interpreted as a larger penetration depth. An example local regime profile in Fig. 4.10, taken from the point $f = 128$ MHz, $E_{dr} = 8 \times 10^4$ V/m in nonlinear mode, shows that the field decay is almost identically exponential.

Fig. 4.9e shows the line $E_{dr} = 5 \times 10^3$ V/m, which shows the anomalous skin effect regime at median frequencies. The linear and nonlinear collisional modes follow the theoretical curve very closely for all frequencies, but the nonlinear collisionless

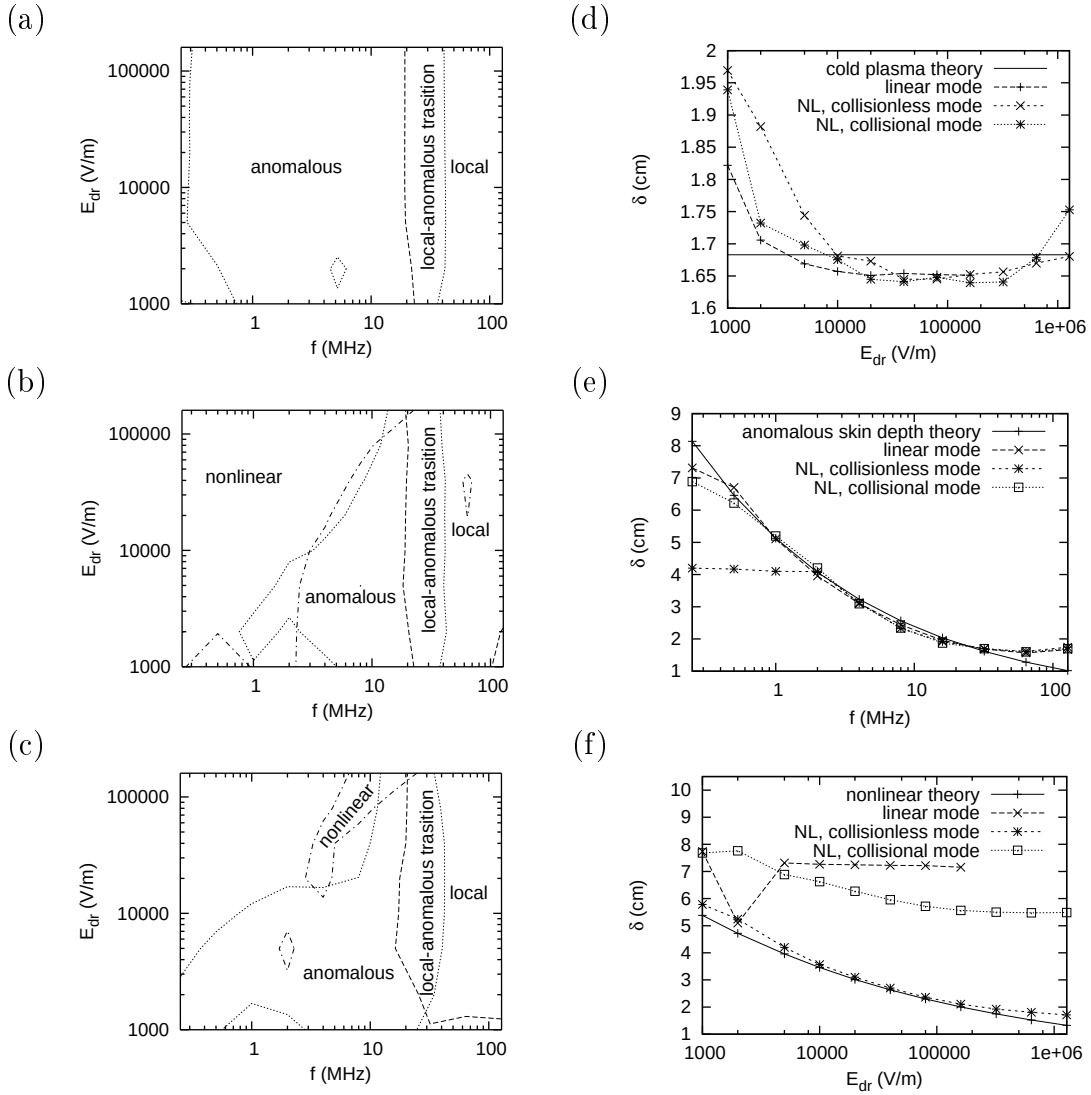

Figure 4.9: The local, anomalous, and nonlinear regimes in the skin depth data are outlined to an error of 10% from theoretical in (a) linear, (b) nonlinear collisionless, and (c) nonlinear collisional simulation modes. The formulae are in Table 2.1. (d) The local skin depth theory and data from all modes along the line $f = 128$ MHz. (e) The anomalous skin depth theory (multiplied by the coefficient 1.6) and data from all modes along the line $E_{dr} = 5 \times 10^3$ V/m. (f) The nonlinear skin depth theory (with $\kappa = \sqrt{\pi}$ and multiplied by the coefficient 2.6) and data from all modes along the line $f = 0.25$ MHz.

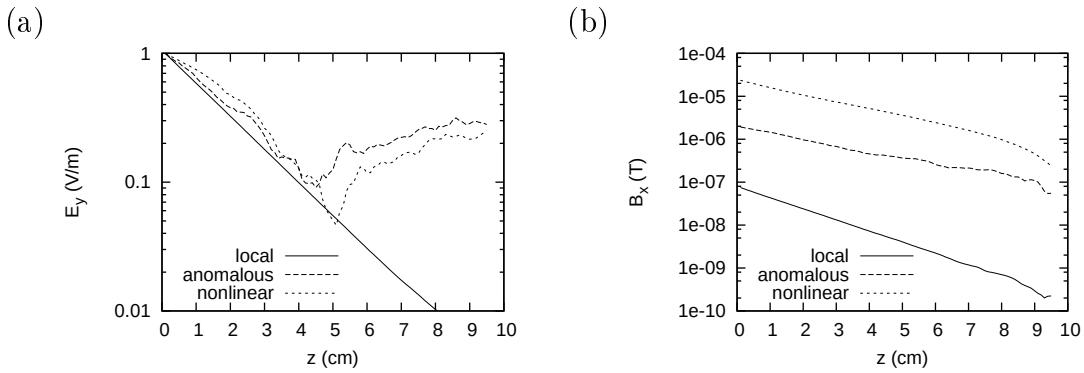

Figure 4.10: The (a) electric and (b) magnetic field profiles from a nonlinear collisionless simulation at three example points: one within the local regime at $f = 128$ MHz, $E_{dr} = 8 \times 10^4$ V/m, one in the anomalous skin effect regime at $f = 4$ MHz, $E_{dr} = 5 \times 10^3$ V/m, and one in the nonlinear regime at $f = 0.25$ MHz, $E_{dr} = 8 \times 10^4$ V/m.

mode deviates below $f = 2$ MHz. An example anomalous skin effect regime profile in Fig. 4.10, taken from the point $f = 4$ MHz, $E_{dr} = 5 \times 10^3$ V/m in nonlinear mode, shows that the thermal effects cause the field decay to become non-monotonic.

Fig. 4.9f shows the line $f = 0.25$ MHz, which falls inside the nonlinear regime for only the nonlinear collisionless mode, for which it matches the predicted theory very well. In linear mode, it falls inside the anomalous skin effect regime, which does not depend on frequency. In nonlinear collisional mode, the data match the nonlinear theory in form, but with a 40% increase in the skin depth. An example nonlinear regime profile in Fig. 4.10, taken from the point $f = 0.25$ MHz, $E_{dr} = 8 \times 10^4$ V/m in nonlinear mode, shows that the field decay is the same as in the anomalous skin effect regime. Nonlinear effects do not change the field profile significantly.

4.7 Behaviour in the Nonlinear Regime

As has previously been shown, the plasma exhibits unique behaviour in the nonlinear regime. As the amplitude of the driving wave is increased, the magnetic field begins to dominate over the thermal effects until the Larmor radius is smaller than either the mean free path of the electrons, or the nonlinear skin depth becomes smaller than the local skin depth. To summarize the effects in the nonlinear regime as the wave amplitude is increased:

- The skin depth is reduced.
- Power absorption weakens.

- The peak absorption frequency increases.

- The PMF at low frequency grows towards its value at high frequency.

Collisional effects serve to cancel the skin depth reduction and PMF increase, but improve power absorption. In addition to these modifications, there are further subtle effects that have not yet been shown.

4.7.1 Kinetic Energy Anisotropy

When the simulation is run in linear mode, the temperature throughout the plasma remains at its initial temperature, with a small uniform increase due to power absorption. However, when the simulation is run in nonlinear collisionless mode, there is a large increase in longitudinal particle motion parallel to the EM wave coupled with a decrease in the transverse particle motion perpendicular to the wave in the nonlinear regime (Fig. 4.11a, b). In fact, at high amplitudes, all transverse motion disappears and there anisotropy. (Fig. 4.11c).

Outside the nonlinear regime, the plasma exhibits a uniform growth in plasma temperature, but inside the increase is restricted to the skin layer and does not occur in the plasma bulk (*e.g.* 128 MHz data in Fig. 4.11a, b). The amplitude of the longitudinal kinetic energy that exceeds the background temperature is directly proportional to the amplitude of the driving wave (Fig. 4.11d), but oscillates at the second harmonic. In the linear mode, there is uniform heating independent of wave amplitude (Fig. 4.11d). The same is true with collisions, except that the heating is much stronger.

4.7.2 High-Order Harmonics

Godyak [4] describes observing the appearance of a spectrum of higher order harmonics of the longitudinal electric field in a cylindrical ICP. These simulations show harmonics that appear in the transverse electric field of planar ICP. Fig. 4.12a shows an example of the difference in form at different frequencies. At high frequency, the transverse electric field in the skin is sinusoidal, but as the frequency decreases, it becomes a triangle wave.

To find the conditions for this phenomenon, rather than testing each harmonic separately to find a spectrum, a pure sinusoid is added to a pure triangle wave using

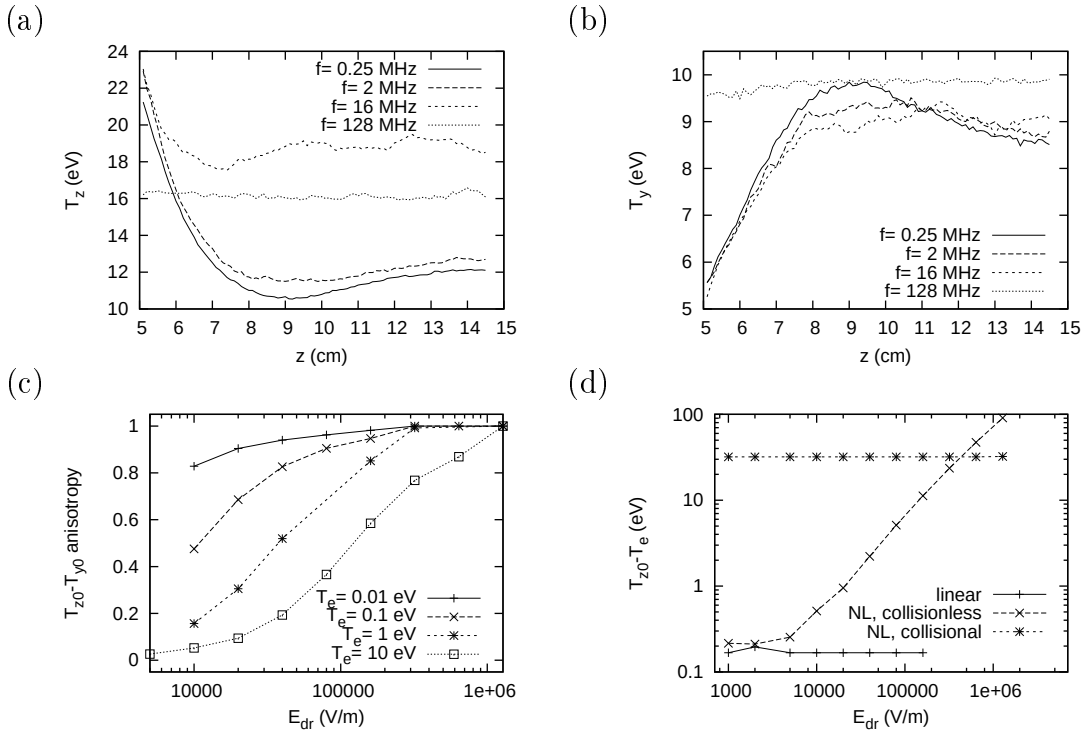

Figure 4.11: (a) The oscillation maximum of the longitudinal kinetic energy T_z throughout the plasma surface. (b) The oscillation minimum of the transverse kinetic energy T_y throughout the plasma. (c) The longitudinal-transverse anisotropy at the surface at different temperatures. (d) The relationship of the energy deviation at the surface from the initial average energy to the driving fields. The plasma starts at temperature $T_e = 10$ eV, is driven at amplitude $E_{dr} = 1.6 \times 10^5$ V/m, and where not specified, has frequency $f = 0.25$ MHz.

(a) (b)

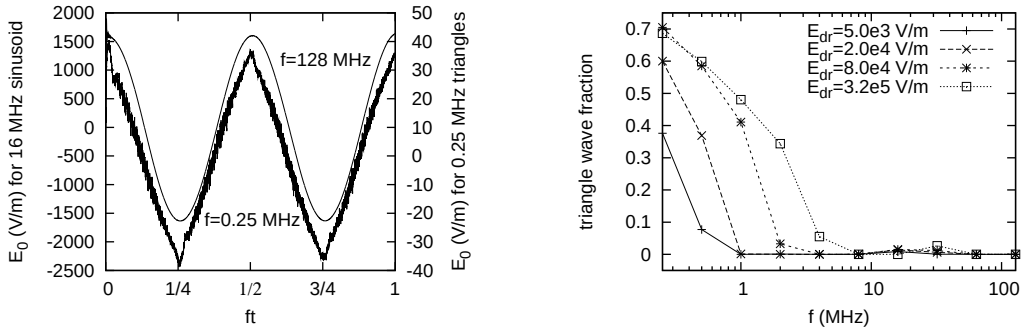

Figure 4.12: Examples of the transverse electric field amplitude at two frequencies, $f = 0.25$ MHz and 16 MHz showing sinusoidal and triangle waveforms. The driving amplitude is $E_{dr} = 160 \times 10^3$ V/m. (b) Fit to a superposition of pure sinusoid and triangle waves using Eq. 4.4. The plasma parameters are $L_{pl} = 10$ cm, $n_e = 10^{17}\,\mathrm{m}^{-3}$, and $T_e = 10$ eV.

a variable mixing fraction. The fit takes the form

$$E_y(z = 2\,\mathrm{mm}, t) = E_0 \left[(1-b)\cos 2\pi f t + b\left(\frac{2}{\pi}\sin^{-1}(\cos 2\pi f t)\right)\right], \quad 0 < b < 1, \tag{4.4}$$

where E_0 is the maximum amplitude of the wave, b is the proportion of triangle wave harmonics to the pure sinusoid. The results in Fig. 4.12b show that the triangle wave comprises a larger portion of the total wave amplitude at low frequency and high amplitude, *i.e.* in the nonlinear regime.

Chapter 5

Discussion

5.1 Temperature Response

When considering the nonlinear collisionless case, the boundaries between regimes of different behaviour are well defined. An important question is how the boundaries between the local, anomalous, and nonlinear regimes change with temperature. To calculate this fully for even three different temperatures would take quite a long time, as many data points covering the frequency-amplitude plane are required to arrive at a smooth contour plot. Therefore, two assumptions are used to reduce the sampling region to a single frequency. The first is that the local and anomalous skin depths are well described by theory at all temperatures, and therefore, the boundary between them is known. The second is that, for constant temperature, the skin depth in the nonlinear regime is independent of frequency (Fig. 4.8c) and related to the magnetic field in the skin layer, and hence also the driving electric field amplitude E_{dr}, by a power law (Fig. 4.7d).

The skin depth in the anomalous skin effect regime is known through linear theory to be $\delta_a \propto T_e^{1/6}\omega^{-1/3}$, while the skin depth in the local regime is a constant. Therefore, as the temperature increases, the anomalous-local boundary moves to higher frequencies. While the skin depth in the nonlinear regime is reduced as the amplitude is increased, it is expected to reach a limit at the cold-plasma value, and therefore, a nonlinear-local boundary should exist at very high amplitudes. From Fig. 5.1a, the skin depth appears to level out at the cold-plasma value, at least for a small range of amplitudes. One can also see that the point at which the skin depth reaches the cold-plasma value increases in amplitude as the temperature grows.

Since the skin depth grows with temperature in both the anomalous and nonlinear regimes, the boundaries between these regimes and the local regime also increase in frequency and amplitude, respectively, when the temperature increases. Conversely, the local regime becomes larger as the temperature drops. This can be seen in Fig.

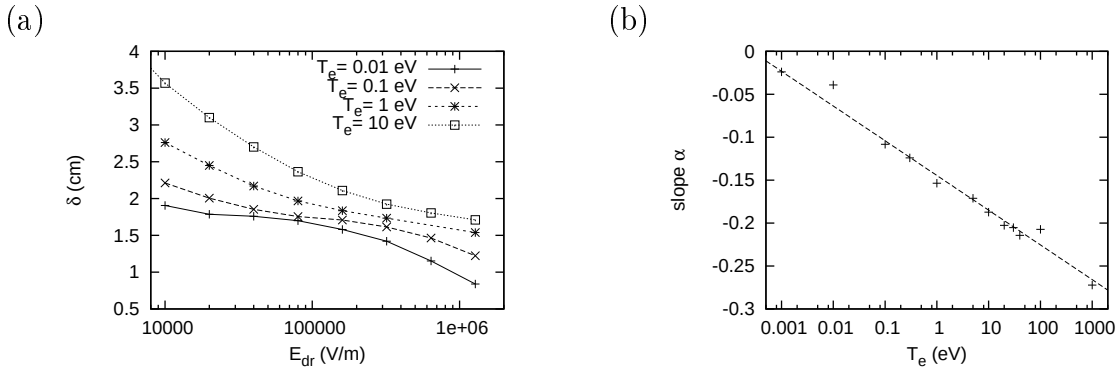

Figure 5.1: (a) The nonlinear skin depth at driving frequency $f = 0.25$ MHz shows a levelling off at the local skin depth $\delta_\omega = c/\omega_{pe} = 1.68$ cm at all temperatures. (b) The dependence of exponent α from Eq. 5.1, which describes the power-law relationship of the skin depth to the electric field.

5.2, which depicts a schematic of the regimes and how they respond to temperature changes.

The final boundary of interest is that dividing the anomalous skin effect regime from the nonlinear regime. The skin depth in the anomalous skin effect regime is known. If the relationship between the skin depth and the field amplitude in the nonlinear regime can be found, then the movement of the boundaries between them can be determined, at least qualitatively. To ensure that the data are acquired well inside the nonlinear regime away from the anomalous skin effect regime, samples are taken from different temperatures at a low frequency of $f = 0.25$ MHz. The results, found in Fig. 5.1a, show that where the skin depth is greater than the cold-plasma value of 1.68 cm, it is related to the driving wave amplitude by a power law.

The exponent of the power law was measured for a number of temperatures, and found to depend on the logarithm of the temperature, so the nonlinear skin depth is proportional to

$$\delta_{nl} \propto E_{dr}^{\alpha \log(T/T_0)}, \tag{5.1}$$

with the parameters $\alpha = -0.018$ and $T_0 = 2.7 \times 10^{-4}$ eV. The value of α determines the amplitude range covered by the nonlinear regime at a given frequency, *i.e.* as the skin depth varies more quickly with the driving electric field, the difference in wave amplitude at the points $\delta_{nl} = \delta_c$ and $\delta_{nl} = \delta_a$ for a given frequency becomes smaller. The critical temperature T_0 is reached when the the stationary sampling points move from the nonlinear regime into the local regime due to boundary movement.

Given the approximate form of the nonlinear skin layer, the boundary line be-

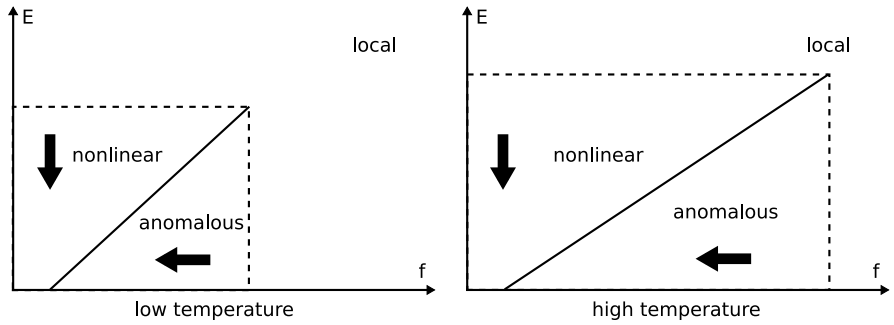

Figure 5.2: The frequency-amplitude plane can be divided into three regimes: local, anomalous, and nonlinear. An increase in temperature decreases the slope of the dividing line between the anomalous and nonlinear regimes and decreases the area of the local regime. Dotted lines indicate gradual transitions. Large arrows indicate the gradient of the skin depth and reverse gradient of the PMF.

tween the anomalous skin effect and nonlinear regimes can be found. The anomalous skin effect regime is related to the temperature via the coefficient $T_e^{1/6}$, whereas the nonlinear regime is related to the temperature through an exponent $E_{dr}^{\alpha \log(T)}$. Therefore, at a high amplitude, a temperature increase will cause the skin depth in the nonlinear regime to grow faster than in the anomalous skin effect regime, but at low amplitude the opposite will occur. Assuming the division between regimes is a straight line (on a logarithmic scale), as it appears to be, then it is expected to rotate in a clockwise direction as the temperature is increased (Fig 5.2). Collisions blur these regime boundaries, which should make them more difficult to discern in an experimental setting.

5.2 Electron Transit Trajectory

The skin depth of the plasma in the nonlinear regime is reasonably well described by Eq. 2.20 at a temperature of $T_e = 10$ eV. However, the dependence of the PMF on temperature in Eq. 5.1 does not match that predicted by Eq. 2.60. It would be desirable to have a more accurate equation for the distance an electron travels inside the skin layer, but since the skin depth depends on the logarithm of the temperature, this rules out a simple dependence on both the Larmor radius and gyro-frequency.

In an attempt to ascertain the source of the nonlinear behaviour, a program was written which tracks the trajectory of individual electrons as they pass through a

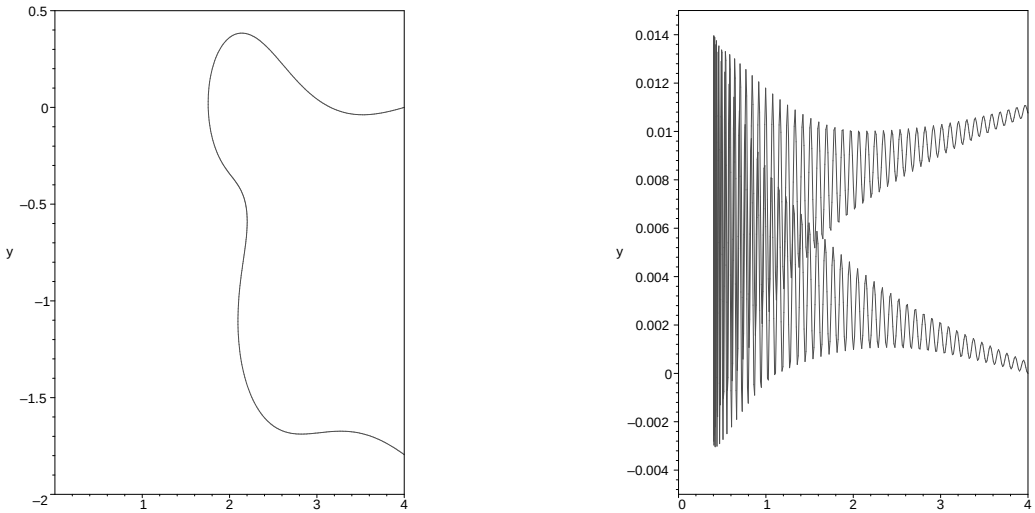

(a) (b)

Figure 5.3: Example trajectories of a charged particle passing through a skin layer with fields given by Eq. 5.2. Distances are normalized to the skin depth. (a) A low frequency test with injection speed $v_{Te} = 20\omega/\delta$ exhibits a long meandering path that strongly depends on injection angle. (b) A high-frequency test with injection speed $v_{Te} = 0.6\omega/\delta$ exhibits a path dominated by the quiver motion that is independent of injection angle.

skin layer with an exponential profile

$$\begin{aligned} E_y &= B_0 \delta \omega e^{-z/\delta} \cos(\omega t + \phi), \\ B_x &= -B_0 e^{-z/\delta} \sin(\omega t + \phi). \end{aligned} \tag{5.2}$$

This is not a self-consistent simulation, as only one electron exists at any one time. The skin depth δ, circular frequency ω, field amplitude B_0, starting phase of the fields ϕ, and injection velocity of the electron are all fixed. The purpose of this investigation is to find whether the electron transit path length through the skin layer can be described by a simple, yet accurate, equation.

The path length of each trajectory strongly depends on the starting parameters. Fig. 5.3 shows the difference between a particularly long meandering path that can occur at low frequency and a rapidly oscillating one that occurs at high frequency. While the skin depth, amplitude, and frequency determine the "genre" of the path, what is more important to its length is the injection angle of the electron and starting phase of the wave. A phase diagram of this dependence for some typical parameters is shown in Fig. 5.4 and it is clearly not a simple relationship. As Pippard predicted for the linear case [14], electrons that enter the skin layer at oblique angles are much

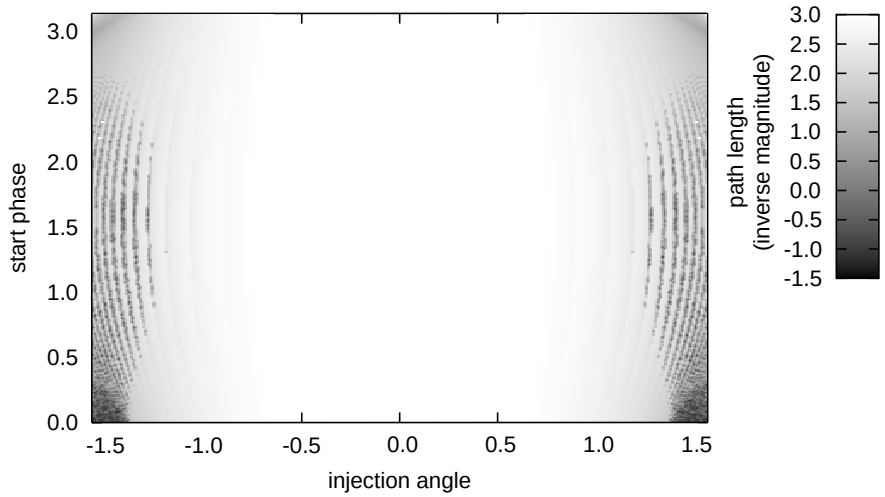

Figure 5.4: A phase plot showing path length of charged particles passing through an exponential skin layer. The fields are given by Eq. 5.2 and the parameters $B_0 = 10^{-4}$ T, $\omega = 1$ MHz, $\delta = 0.02$ cm, and start phase ϕ. Each particle is injected with speed $v_{Te} = 10^6$ m/s at the specified injection angle as measured from normal. Dark structures show long trajectories.

more likely to remain there over a long distance. Unfortunately, there is a finely detailed structure separating very long path lengths from very short ones (Fig. 5.4).

To sidestep this complication, the space of injection angle and starting wave phase is sampled at a high resolution, and the path lengths are averaged together. Weights are assigned according to the injection speed normal to the skin layer:

$$< l_{path} >= \frac{\sum_i v_z l_{path}}{\sum_i v_z}, \tag{5.3}$$

where l_{path} is the path length summed over each i particle. In an isotropic distribution, particles with velocity close to normal transit the skin layer more frequently than those that enter at oblique angles. Using this method, the same region sampled with the PIC program was investigated with this simpler tool.

By averaging over the parameters of electron entry into a prescribed skin layer, only the trajectory details that are electron independent and occur even without self-consistent fields are present. The time spent in the skin layer (Fig. 5.5a, b) increases as the frequency is reduced, except in the presence of weak fields, where an electron will just strike the boundary and be reflected back out of the skin layer. The path length is completely independent of the travel time (Fig. 5.5c, d). It grows exponentially as the amplitude is increased and frequency decreased simultaneously,

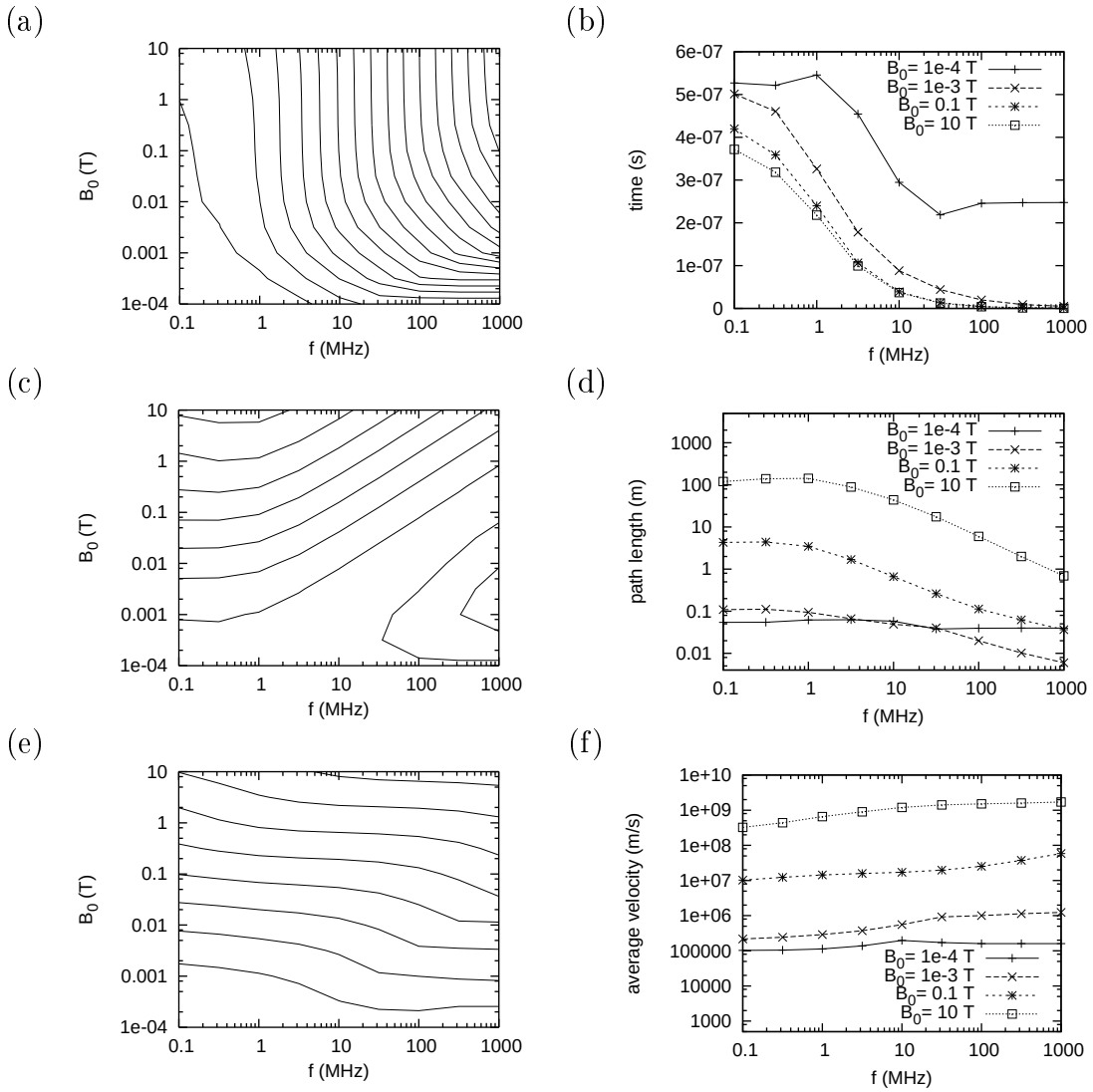

Figure 5.5: (a,b) The time of flight, (c,d) trajectory length, (e,f) and average velocity averaged over all electrons with initial speed $v_{Te} = 10^5$ m/s that pass through an exponential skin layer of depth $\delta = 2$ cm in a plasma of density $n_e = 10^{17}\,\mathrm{m}^{-3}$:

such that the contour lines appear to be parallel to the nonlinear regime boundary.

The average velocity the electrons have while traversing the skin layer (Fig. 5.5e, f) is almost independent of the frequency. The average velocity also increases with the PMF in the nonlinear regime. The average velocity grows exponentially with field strength starting from the initial speed of the particle. However, the rate of increase does not change with temperature, indicating that the cause of the temperature dependence in the nonlinear regime is not the result of single particle behaviour.

5.3 Cause of the Nonlinear Regime

The plasma is highly reflective in the nonlinear regime, while the skin depth and PMF are proportional to the amplitude of the driving wave. From the self-consistent simulation, as well as by sending single electrons through an exponential skin layer, it is also known that the average of their velocity in the skin layer is proportional to the field amplitudes. This suggests that electrons are storing wave energy as kinetic energy, which is contained by the cyclotron motion until they are slowed down when the fields reverse direction. This hypothesis is further corroborated by the oscillating kinetic energy that is localized in the skin layer.

It is possible that the different regimes are defined by the most efficient method for plasma relaxation. The local regime reflects the wave by electron quiver motion. The nonlinear regime reflects it by storing energy kinetically, but keeping it localized via gyration until it can be ejected. The anomalous skin regime absorbs the wave energy and heats the plasma, since the electrons cannot quiver fast enough and the magnetic field is not strong enough to enforce full orbits.

5.4 Open Questions

Aspects of ICP behaviour that have the potential for continued study include the effect of mobile ions, better detail regarding temperature changes and collision rates, and the effect of applied fields. Mobile ions were purposely ignored for most of this work in favour of rapid data acquisition. While their omission was proved to be inconsequential for most of the tests, a future study should determine the period required for ions to reach equilibrium in the skin, and adjust the diagnostic functions accordingly. The dependence of the plasma on temperature and electron-neutral collision rate was measured for only a small set of values and extrapolated to arrive at general results. In addition, the method by which the nonlinear regime

is eliminated by collisions is not completely explained. Finally, the PIC program has the capability of simulating externally applied magnetic fields, a feature common to physical devices, but not investigated in this work.

5.5 Conclusion

As predicted for linear mode, all plasma properties were found to be independent of wave amplitude. At high frequencies the plasma is in the local regime, which exhibits a short skin depth, high reflectivity, and strong PMF. These remain constant even as the frequency is further increased. At low frequencies the plasma is in the anomalous skin effect regime, the skin depth increases with frequency and the PMF weakens; the plasma enters the anomalous skin effect regime caused by thermal motion. In this regime, the power absorption increases with frequency, and therefore peaks at the transition between the local and anomalous skin effect regimes.

In nonlinear collisionless mode, the plasma becomes dependent on the driving power. The local regime remains unchanged, but the anomalous skin effect regime exists only at low frequencies and amplitudes, where the magnetic field is weak. The nonlinear regime appears at low frequencies and high amplitudes where the magnetic field is strong. Numerous interesting effects occur in the nonlinear regime: the skin depth increases with the input power, while the ponderomotive force decreases correspondingly, but both are independent of driving frequency. The plasma also becomes highly reflective, the transverse electric field takes on a triangular waveform, and the particle motion in the skin layer becomes anisotropic, but the degree of anisotropy oscillates at the second harmonic with the PMF.

The presence of the nonlinear regime is explained by magnetic trapping: as the magnetic field becomes strong, the electrons begin to gyrate in orbits with smaller Larmor radii. With the assumption that the length of the orbit inside the skin layer is an effective mean free path, the skin depth in the nonlinear regime was successfully predicted. Because the Larmor radius of the electrons decreases as the amplitude of the driving wave increases, at very high amplitudes the radius becomes small enough for the plasma to recover local behaviour.

In nonlinear collisional mode, the reflectivity of the plasma is increased under all conditions. The introduction of particle collisions improves energy absorption and effectively eliminates the nonlinear regime and its distinct phenomena. However, there is still some amplitude dependence, and the anomalous skin effect regime retains the same boundaries as in nonlinear collisionless mode.

The transition boundaries between regimes change as a function of temperature, with the parameter range of the anomalous skin effect regime increases with temperature. In linear mode, heating the plasma causes the boundary between the local and anomalous skin effect regimes to move to higher frequencies. In nonlinear collisionless mode, heating the plasma the same, but also causes the boundary between the local and nonlinear regimes to move to higher wave amplitudes and the boundary between the nonlinear and anomalous skin effect regimes to decrease slope in amplitude-frequency space so that the anomalous skin effect regime covers a greater range at low amplitudes.

References

[1] C.K. Birdsall and A.B. Langdon. *Plasma Physics via Computer Simulation*. Institute of Physics Publishing, Philadelphia, 2001.

[2] F.F. Chen. Collisional, magnetic, and nonlinear skin effect in radio-frequency plasmas. *Physics of Plasmas*, 8(6):3008–3017, 2001.

[3] B.D. Fried and S.D. Conte. *The Plasma Dispersion Function*. Academic Publishing, New York, 1961.

[4] V. Godyak. Plasma phenomena in inductive discharges. *Plasma Physics and Controlled Fusion*, 45:A399–A424, 2003.

[5] G. Joyce, M. Lampe, S. Slinker, and W. Manheimer. Electrostatic particle-in-cell simulation technique for quasineutral plasma. *Journal of Computational Physics*, 138(2):540–562, 1997.

[6] A.H. Karp and H.P. Flatt. Measuring parallel processor performance. *Communications of the ACM*, 33(5):539–543, 1990.

[7] V.I. Kolobov and D.J. Economou. The anomalous skin effect in gas discharge plasmas. *Plasma Sources Science and Technology*, 6(2):R1–R17, 1997.

[8] L.D. Landau and E.M. Lifshitz. *Electrodynamics of Continuous Media*. Pergamon Press, New York, 1984.

[9] A.B. Langdon. Effects of the the spatial grid in simulation plasmas. *Journal of Computational Physics*, 6(2):247–267, 1970.

[10] M.A. Lieberman and A.J. Lichtenberg. *Principles of Plasma Discharges and Materials Processing*. Wiley Interscience, Hoboken, 2005.

[11] E.L. Lindman. Dispersion relation for computer-simulated plasmas. *Journal of Computational Physics*, 5(1):13–22, 1970.

[12] H. London. The high-frequency resistance of superconducting tin. *Proceedings of the Royal Society A*, 176(A967):522–533, 1940.

[13] H. Okuda. Nonphysical noises and instabilities in plasma simulation due to a spatial grid. *Journal of Computational Physics*, 10(3):475–486, 1972.

[14] A.B. Pippard. The surface impedance of superconductors and normal metals at high frequencies .2. the anomalous skin effect in normal metals. *Proceedings of the Royal Society A*, 191(1026):385–399, 1947.

[15] K.C. Shaing. Electron heating in inductively coupled discharges. *Physics of Plasmas*, 3(9):3300–3303, 1996.

[16] K.C. Shaing and A.Y. Aydemir. Collisionless electron heating in inductively coupled discharges. *Physics of Plasmas*, 4(9):3163–3166, 1997.

[17] A.I. Smolyakov, V. Godyak, and Y. Tyshetskiy. Effect of the electron thermal motion on the ponderomotive force in inductive plasma. *Physics of Plasmas*, 8(9):3857–3860, 2001.

[18] M. Surendra, D.B. Graves, and G.M. Jellum. Self-consistent model of a direct-current glow-discharge - treatment of fast electrons. *Physical Review A*, 41(2):1112–1125, 1990.

[19] D. Sydorenko. *Particle-in-cell simulations of electron dynamics in low pressure discharges with magnetic fields*. PhD thesis, University of Saskatchewan, 2006.

[20] M.M. Turner. Collisionless electron heating in an inductively-coupled discharge. *Phys. Rev. Lett.*, 71(12):1844–1847, 1993.

[21] Y.O. Tyshetskiy, A.I. Smolyakov, and V.A. Godyak. On nonlocal heating in inductively coupled plasmas. *Plasma Sources Science and Technology*, 11(2):203–207, 2002.

[22] Y.O. Tyshetskiy, A.I. Smolyakov, and V.A. Godyak. Reduction of electron heating in the low-frequency anomalous-skin-effect regime. *Physical Review Letters*, 90(25):255002, 2003.

[23] V. Vahedi and M. Surendra. A monte-carlo collision model for the particle-in-cell method - applications to argon and oxygen discharges. *Computer Physics Communications*, 87(1-2):179–198, 1995.

[24] E.S. Weibel. Anomalous skin effect in a plasma. *Physics of Fluids*, 10(4):741–748, 1967.

[25] N.S. Yoon, S.S. Kim, C.S. Chang, and D. Choi. One-dimensional solution for electron heating in an inductively coupled plasma discharge. *Physical Review E*, 54(1):757–767, 1996.